The University of Southern Queensland

Faculty of Health, Engineering and Sciences

Spectral Proper Orthogonal Decomposition of High Speed Schlieren Images

A dissertation submitted by

Adam Smith

in fulfilment of the requirements of

ENG4111 and ENG4112 Research Project

towards the degree of

Bachelor of Engineering (Honours) (Mechanical)

Submitted: October 2023

Abstract

Sustained hypersonic flight will enable travel between cities in a few hours however, there are many problems to be solved such as control of the boundary layer state. The University of Southern Queensland's hypersonic testing facility regularly conducts experiments and research of hypersonic boundary interactions. The facility can be configured for a Ludwieg tube with free piston compression heating, or an atmospheric pressure blow down to vacuum operation. The facility is capable of producing hypersonic flows from Mach 2 to Mach 7 for approximately 200 ms.

High speed schlieren images of the flow field of the test section was obtained and Spectral Proper Orthogonal Decomposition (SPOD) was utilised to investigate the flow around a 7-degree half angle precision machined cone mounted in the test section with a zero angle of attack. The schlieren images captured at 450,000 fps was used to investigate the most energetic modal frequency and modal shapes/structures. The SPOD results were compared to high-speed surface pressure fluctuations which are measured at discrete locations along one azimuthal ray of the model surface.

The SPOD technique was unable to resolve the power spectrum to be consistent with the established pressure fluctuation measurements. However, the SPOD frequency image analysis was able to identify the second-mode instability. These image results suggest that SPOD could be used to study boundary layers in TUSQ. Such further studies should involve the acquisition of a high-speed camera capable of >450,000 fps. Ideally, a frame rate of at least 560,000 fps should be investigated.

University of Southern Queensland

Faculty of Health, Engineering & Sciences

Certification of Dissertation

I certify that the ideas, designs and experimental work, results, analysis and conclusions set out in this dissertation are entirely my own effort, except where otherwise indicated and acknowledged.

I further certify that the work is original and has not been previously submitted for assessment in any other course or institution, except where specifically stated.

Adam Smith

▇▇▇▇▇▇▇

▇▇▇▇▇▇

_____
Signature

    12/10/2023
_____
Date

Acknowledgements

As this draws a close to my academic education, I have taken a moment to reflect on what I have achieved in my journey. To fulfil a dream of becoming an engineer whilst providing for my family was a challenging task and, I acknowledge the University of Southern Queensland for this opportunity. I must firstly thank my supervisor of this research. Byrenn, your guidance, support and understanding throughout this research has been invaluable. Regardless of your workload throughout the past year, you never hesitated to make the time to catch up or nearly instantly reply when asked for advice. Your extensive knowledge of MATLAB and TUSQ was invaluable in the completion of this thesis, and I am grateful for your contribution.

I acknowledge the understanding of my son, Aiden. From the moment he could understand, he has witnessed his dad reading a textbook or spending a Sunday working on an assignment. I look forward to life with him after study and I hope my journey proves as an inspiration to always follow your dreams.

Lastly, I thank my wife, Felicity. My journey began as a diploma and concludes as an honours degree. Her motivation and understanding to accept me pursuing my degree is one of a kind and I will forever be grateful for her actions of encouragement and her ability to keep me focused, no matter how disrupted life became.

Table of Contents

List of Figures

List of Tables

Nomenclature

c	Speed of sound (m/s)
A	Cross-sectional Area (m^2)
M	Mach number
P	Pressure (Pa)
R	Ideal gas constant (J/kg K)
Re	Reynolds Number
T	Temperature (K)
V	Velocity (m/s)
k	Ratio of specific heats
μ	Mach Angle (°)

Acronyms

CNC   Computer Numerical Control

DMD   Dynamic Mode Decomposition

fps   frames per second

PCB   Printed Circuit Board

POD   Proper Orthogonal Decomposition

PSD   Power Spectral Density

SWBLI   Shock Wave/Boundary Layer Interaction

SPOD   Spectral Proper Orthogonal Decomposition

TUSQ   UniSQ Hypersonic Wind Tunnel

Chapter 1

Introduction

1.1   Project Aim

This project is motivated by the desire to extend the experimental capabilities in the University of Southern Queensland's Hypersonic Wind Tunnel (TUSQ) to transition research supported by non-intrusive diagnostics. In this case, schlieren imaging is the most used optical diagnostic in TUSQ, so should have a relatively low barrier of entry to researchers. The Spectral Proper Orthogonal Decomposition (SPOD) technique investigated requires no additional equipment however, upgraded equipment would be beneficial. My involvement in this project began through the manufacture of the test model which provides the foundation for this research.

The project aim is to use spectral proper orthogonal decomposition (SPOD) for the investigation of the flow around models which are mounted in the University of Southern Queensland's Hypersonic Wind tunnel (TUSQ). The primary objective is to apply the SPOD technique to the study of second-mode instabilities, imaged using high-speed schlieren, in the boundary layer of a slender cone at Mach 6. The analysis should reveal the most energetic modal frequency and structures. The SPOD results will be compared to high-speed surface pressure fluctuations which are measured at discrete locations along the one azimuthal ray of the model surface.

Utilising a non-intrusive method such as schlieren with SPOD analysis to investigate the boundary layer state over an area offers advantages over the established point measurement using surface pressure transducers such as: (1) a near-continuous measurement of the spatial evolution of the boundary layer; (2) no flat surfaces being introduced by the pressure transducers; and (3) no change of the surface finish at the sensor location.

1.2　Dissertation Outline

An outline of the dissertation chapters is outlined below:

- **Chapter 2** Describes a fundamental background on hypersonic theory and concludes on discussion of current literature.
- **Chapter 3** Describes the methodology of the project with details on the facility, experimental model and imaging analysis used with experimental analysis in hypersonic flow techniques to be applied.
- **Chapter 4** Discusses the results of the project including annotations and findings.
- **Chapter 5** Discusses the authors conclusion of their work and further work opportunities.

Chapter 2

Literature Review

2.1   Chapter Overview

This Chapter presents a fundamental background of hypersonic theory. The chapter concludes on current literature and gaps observed in current work in within boundary layer interactions and spectral analysis.

2.2   Hypersonic Fundamentals

The analysis of compressible gas that involves systems with high speed flows is generally expressed as a dimensionless number known as the Mach number. Cengel et al. (2017) defines the Mach number as

$$Ma = \frac{V}{c}$$

Equation 1

Where V is the velocity of air and c is the local speed of sound. The speed of sound is a function of temperature only and is defined as

$$c = \sqrt{\gamma RT}$$

Equation 2

Where γ is the ratio of specific heats, $R \left(\frac{J}{kgK} \right)$ is the gas constant and $T\ (K)$ is the temperature of the fluid (Pritchard 2011).

A flow is called hypersonic when the $Ma \gg 1$ (Cengel et al. 2017). Anderson (1984) states that the conventional definition of hypersonic flow within the industry is where the Mach number is greater than 5 however, notes that this is a rule of thumb. Hypersonic flow is more accurately described as where certain flow phenomena become progressively more dominant as the Mach number increases. The following phenomena constitutes a description of features which are present in accurate definition of hypersonic flows.

2.2.1   Thin Shock Layers

The theory of oblique shock states that there is a notable increase of density along the shock wave, progressively increasing with respect to a larger Mach number. Once the density increases, it allows the mass flow following the shock to easily pass small voids. If the body is experiencing hypersonic flows the distance that is observed between the body and the shock wave can be thin. This is defined as the shock layer (Anderson 1984).

2.2.2   Entropy Layer

In a hypersonic flow, a thin shock layer is observed over a blunt nose with small shock detachment along the body. This creates a curve within the shock wave leading to large amounts of entropy in the body layer. Entropy flows downstream of the body, a phenomena known as wetting the body. Problems exist due to this as it becomes difficult to perform boundary calculations due to the unknown edge conditions of the boundary layer (Anderson 1984). Because of the presence of the entropy layer, studies of second-mode instabilities in hypersonic flows are conducted on sharp-nosed models.

2.2.3   Viscous Interaction

Increased kinetic energy dissipates within the boundary layer in a hypersonic flow causing large increases in temperature. This increase causes an increase in the viscosity coefficient and a reduction in density. The thickness of the boundary layer increases, causing additional flow inconsistency by interacting with the outer inviscid flow creating a viscous interaction phenomena.

2.2.4   High Temperature Flows

The viscous dissipation as described in viscous interaction generates high surface temperatures. This can lead to vibrational excitation and dissociation. In hypersonic flow, the boundary layer chemical reaction extends to the reacting flow of the shock layer therefore, influences parameters such as lift, drag and moments on the vehicle (Anderson 1984). However, since hypersonic flows can be produced in ground based test facilities at less than flight enthalpy, there is a need to separately classify hypersonic flows at high and low enthalpy. For flows greater than Mach 5 the term hypersonic is used. Flows greater than Mach 5 where the enthalpy is high such that high-temperature effect must be considered are termed hypervelocity flows.

2.2.5   Summary

As the Mach number increases to higher values, some or all of the discussed phenomena become more apparent in defining hypersonic flow. A visual representation of these characteristics is shown in Figure 1.
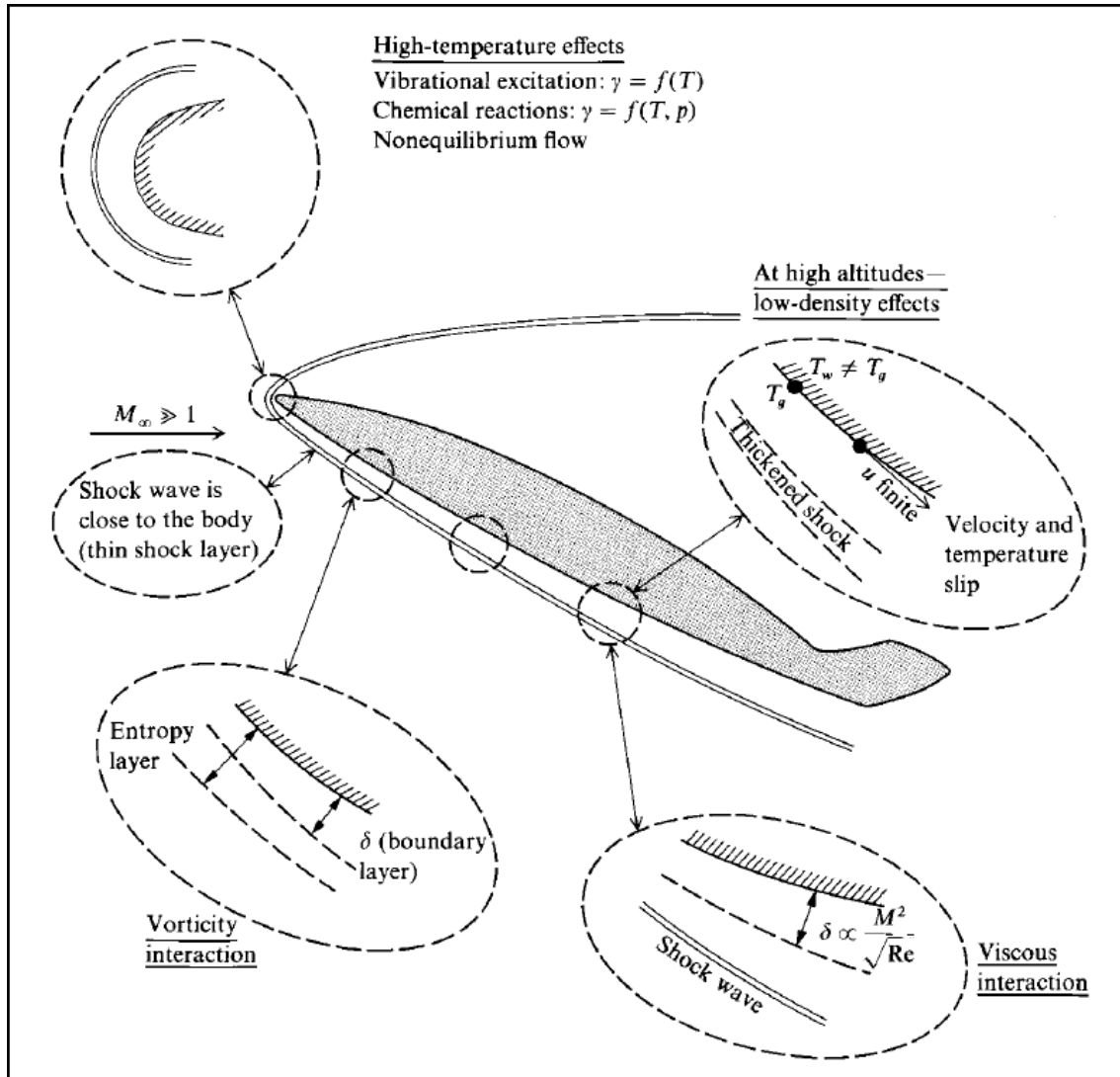
Figure 1. Visual representation of hypersonic flow parameters (Anderson 1984)

2.3   The Second Mode Instability

Second mode disturbances can be physically categorised as trapped acoustic waves located within the boundary layer. This is a generalised description however, the validity remains only under very strict particular and often, unrealistic circumstances (Knisely & Zhong 2019). It was concluded by Kuehl (2018) that thermoacoustic interpretation of the second mode dynamics are consistent with that of a forced, resonating, thermoacoustic standing trapped in a thermoacoustic impedance well.

Second mode disturbances propagate downstream and have a phase speed similar to the velocity of the boundary layer edge velocity with a wavelength that can be up to three times the thickness of the boundary layer. This produces dominant frequencies ranging from approximately 100 kHz to greater than 1 MHz (Laurence et al. 2016).

It is common to conduct research of hypersonic boundary layer transition on 7-degree half-angle cones as the simple geometry leads to verification of characteristics. This provides confidence in the technique to further test more complex geometries (Hyslop et al. 2021) When the study of second mode instabilities is of primary interest, the nose cone should be manufactured with a near sharp intersection point. This will avoid the formation of a significant entropy layer which can lead to suppression of the second mode instability (Kuehl 2018).

A schematic that illustrates the boundary layer path transition is shown in Figure 2. If the environment consists of a weak disturbance, three stages of the path to transition exists. This consists of: (1) receptivity; (2) linear eigenmode growth; and (3) nonlinear breakdown to turbulence. The process of receptivity translates the external forces into boundary layer waves providing the initial condition of phases, frequencies and amplitudes. Modal growth remains linear of the unstable boundary layer waves. This can be obtained by calculating the eigenvalue equations of the homogeneous linearised stability equations. However, the cause of the break down to turbulence is primarily from the nonlinear secondary instability when the boundary layer waves reach certain amplitudes.

This three-stage process of transition is represented as path A in Figure 2 (Zhong & Wang 2012).

As there is growth in the disturbance amplitude, transient growth from the nonorthogonal nature of Orr-Sommerfeld and Squire eigenvalues increases importance. A weak transient growth can provide an increased initial amplitude contributing to modal growth. This has been represented as path B in Figure 2. However, if the transient growth is strong, this can directly lead to nonlinear instabilities further, resulting in a breakdown to turbulence. This is represented as path C and D in Figure 2. In the context of hypersonic boundary layers, the first and second modes are the relevant instability waves although, second mode instability becomes the most dominant instability with Mach numbers larger than 4 (Zhong & Wang 2012).
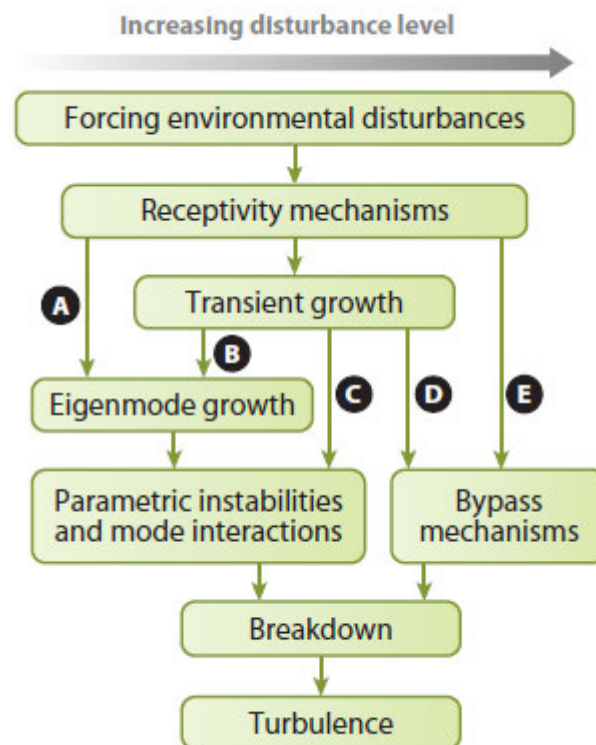
Figure 2. A schematic of the boundary layer transition path to turbulence (Iyer 2015)

2.4 Shock   Wave   Boundary   Layer   Interaction Unsteadiness

SPOD has been successfully applied to shock wave boundary layer interaction (SWBLI) studies in hypersonic flows therefore, it is advantageous to explore the properties of SWBLI to discover and similarities which may exist with the study of the second mode instability. SWBLI unsteadiness has been directed to either completely turbulent or laminar boundary layers (Gaitonde 2015). Generally, interactions within the turbulent and laminar boundary layer maintain symmetric with respect to the test plate centreline and is seen as a smooth separation line as shown in Figure 3 (a) and (c). However, a laminar boundary interaction develops large separation bubbles (Murphree et al. 2006). Traditionally, it is observed that a transitional interaction will include both phenomena as seen in a turbulent or laminar flow.
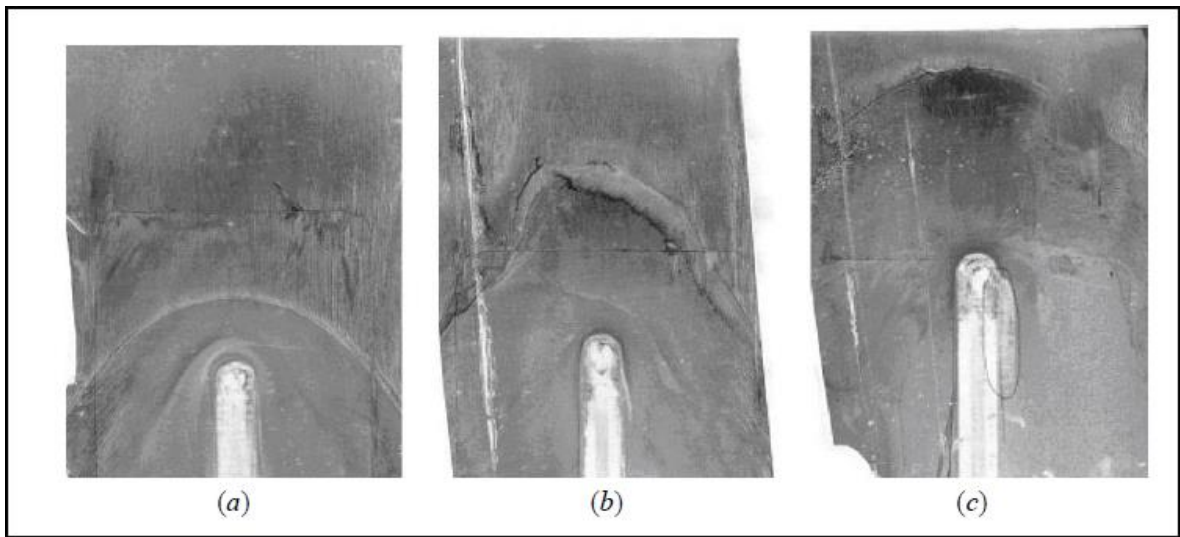
Figure 3. An example of streakline visualisation in hypersonic flow by (a) fully turbulent, (b) transitional, (c) laminar (Murphree et al. 2006)

In past studies, literature has emerged that offers contradictory theories on the cause of SWBLI. It has been published that there is no influence from the upstream boundary layer and that it is the downstream separation bubble that promotes unsteadiness (Martin et al. 2008). However, it has been argued that the driving cause of unsteadiness is the upstream boundary layer.

Furthermore, Combs et al. (2017) suggests that both upstream and downstream boundary layers could contribute with the conditions of each becoming more apparent with respect to the conditions of the flow.

Utilising the process of schlieren images and pressure measurement, shock waves in the boundary layer has been investigated in a transitional flow. With the aid of a shock generator, interactions were produced. It was observed that a low frequency fluctuation occurred at separation and reattachment points. Occurring at a high frequency, this suggests that the upstream boundary layer is a critical factor in low frequency SWBLI unsteadiness (Estruch et al. 2010).

Clemens and Narayanaswamy (2014) published their results of a study of past research that studies low frequency unsteadiness within the shock wave boundary layer interaction. They concluded that the upstream boundary layer works in a combination with downstream instability in all the interactions. It was observed that the extent unsteadiness was directly related to the upstream boundary layer and that a decrease was observed when the separation bubble increased.

A recent study by Combs et al. (2016); Combs et al. (2017) was conducted on SWBLIs that are cylinder induced. Both transitional and fully turbulent flows were observed. With the aid of SPOD analysis, the high speed schlieren images showed that there was increased energy within the separated flow region. This was observed in the 2 kHz – 6 kHz band within the transitional boundary layer interaction. However, separated flow was not observed in the spectral analysis of a turbulent boundary layer interaction although, the schlieren image showed that separated flow was visible in the interaction. This concluded that the unsteadiness observed in a transitional interaction is influenced by the instability of the separated flow region however, the turbulent interactions are observed from the incoming boundary layer (Cottier 2019). Therefore, spectral decomposition methods such as SPOD have been utilised to successfully identify modes and structures containing energy within SWBLI applications from schlieren measurement. As these applications utilise schlieren imaging, the density gradient of the flow in one direction is utilised as per the intended application to the second mode instability.

A significant difference between SWBLI and second mode applications is the frequency of application. SWBLI the energy containing modes and within the order of kHz while the second mode is present in the 100s of kHz bands. The increased frequency is essentially a higher wavenumber and therefore, a smaller structure. Applying the method of SPOD to the study of the second mode instability will analyse the limitations of SPOD both spatially and spectrally.

2.5   Application   of   Modal   Decomposition   to   to Studies of Hypersonic Boundary Layers and SWBLI

The stability and transition from laminar to turbulent boundary layers at hypersonic speed has maintained an interest in academic research for over 50 years. First and second mode boundary instabilities are associated with the path to turbulence particularly, in dominant modal growth (Fedorov 2011). Mack (1975) confirmed that boundary instability is a prerequisite of transition further noting that altering the frequency and amplitude of the instability varies the transition region. A common technique used to study hypersonic boundary layers is the application of modal decomposition to SWBLI.

Previous research to investigate SWBLIs has focused on alternative methods of modal analysis. However, proper orthogonal decomposition (POD) and dynamic mode decomposition (DMD) are the most widely used methods (Kunihiko et al. 2017). Lumley (1967) initially introduced the theory of POD in the mid 1960's. At that time, POD was utilised as a method of decomposing the turbulent fluid motion into a finite number of modes.

This method was used to capture the energy in the flow field (Weiss 2019). Academics within the hypersonic and fluid transfer disciplines utilised this method, adapting it to increase its ability such as Sirovich (1987) who modelled snapshot POD and Ramasamy et al. (2019) who more recently optimised a clustering technique using POD methodology.

Due to the simplicity in the computational process and the appealing ability of reconstruction of fluid flow phenomena, the POD method maintains relevancy within industry (Weiss 2019). In 2008, Schmid (2010) introduced another now, common method for analysis known as dynamic mode decomposition. This method acts to reduce time resolved data into smaller modes. In a difference with DMD, the modes are listed by a frequency however, POD lists by energy.

Therefore, both methods compute the energy at a single frequency. This promotes sensitivity in the data with respect to noise and small scale turbulence promoting some difficulty in the identification of the correct flow phenomena in some projects (Kunihiko et al. 2017).

A study was conducted on the examination of an oblique shock wave/turbulent boundary layer interactions by Nichols et al. (2016). The DMD and the global stability analysis (GSA) methods were used. The conclusion was that two mechanisms exist to drive instability, the lower frequency motion of the separation bubble and a higher frequency motion much like a wave about the sonic line.

A further study conducted by Priebe et al. (2016) consisted of an observation of the compression ramp induced shock wave/turbulent boundary layer. It was concluded that a factor of frequency unsteadiness could be contributed by a shear layer. Loginov et al. (2006) and Floryan (1991) concluded that although the incoming boundary layer could be influential in large unsteady vortical structures, their results show that the formation is found within the downstream flow. Furthermore, it is thought that the concave streamline contributes to the onset of Görtler vortices that then drive a low frequency unsteadiness.

Vanstone and Clemens (2019a, 2019b) analysis using the POD method showed that there were multiple mechanisms present that drove unsteadiness through different frequencies. Midfrequency unsteadiness was driven by the observation of velocity superstructures in the boundary layer. This was the cause of velocity structures in the separation region. Furthermore, high and low velocity structure in the separation field was likely to be relatable to high frequency unsteadiness. No further conclusions were made with respect to low frequency unsteadiness. However, it was noted that low steady frequencies did was not observed to be controlled but the boundary layer superstructures.

2.6 Review of Spectral Analysis

POD and DMD methods of analysis provide the researcher with greater understanding of the problem. POD modes are ranked with respect to their energy and produce spatially coherent modes however, the time dependence is random. DMD modes are ranked by their frequency therefore, temporally orthogonal. Identifying flow phenomena can be tedious as the energy is also recorded at a singular frequency (Lumley 1967). There has been previous research of the adaptability of combining the spatial orthogonality of the POD method with the temporal orthogonality of the DMD method.

Cammilleri et al. (2013) was involved in a development of an algorithm that obtained dynamics of reduced order model in the means of performing matrix multiplication. This method was known as the Chronos-Koopman Spectral analysis, it utilised the POD and DMD method. The method involved extracting the POD temporal coefficients by applying the Navier Stokes equations followed by performing DMD analysis on the POD chronos. However, this resulted in unreliable results (Cottier 2019).

Another analysis method known as spectral proper orthogonal decomposition (SPOD) has shown to be advantageous (Tinney & Jordan 2008). SPOD uses a Fourier transform that is capable of producing coherent like structures similar to POD analysis however, temporal orthogonality is retained similar to DMD. The SPOD method has been in existence in vary methods since the 1960s however, since the modern advancements of computational power, it has increased in interest within the field (Towne et al. 2018).

Picard and Delville (2000) applied a spectral POD analysis method on unsteady structures combined with a subsonic jet. It was found that the analysis showed SPOD enhanced the temporal wavelength variations as opposed to the POD method. When at its lowest, the SPOD mode contained greater energy than to the compared lowest order POD mode. Similar results were also obtained in an analysis of velocity data of a hot wire rake suggesting that SPOD is a valuable energy analysis method (Tutkun & George 2017).

Proper Orthogonal decomposition (POD) technique remains the most utilised method of analysis. This technique decomposes the modes, generating the spatial correlation tensor. The decomposition process formulates spatially orthogonal modes where the loss of sequential ordering is observed. Therefore, the modes have a random time dependence (Towne et al. 2018). Dynamic Mode Decomposition (DMD) is an alternative analysis technique to POD. DMD was developed to identify coherent structures from the flow data with a primary aim to obtain modes that describe the flow dynamics. However, opposite results are achieved as DMD results in temporal orthogonalization of the data that is spatially non-orthogonal. Where, POD is described as spatially orthogonal modes arranged in a random time dependency (Towne et al. 2018).

In a more recent study, the turbulence of a jet was analysed using the SPOD method by Schmidt and Towne (2019), the study included plotting the Eigenvalue decomposition. This identified a low rank dynamic a lower order mode while over low frequencies. The previous studies have provided a detailed overview into the ability of the SPOD method including, the effectiveness for the application of unsteady flow phenomena. Therefore, SPOD has been selected for this study.

Chapter 3

Methodology

3.1   Chapter Overview

This chapter describes the equipment required for experimental testing. The beginning of the chapter provides an overview of the TUSQ facility at the University of Southern Queensland. This is followed by a description of the manufacturing process of the experimental model and an overview of experiment design is discussed.

The chapter concludes by describing the technique chosen for the work in this project. A fundamental summary of the SPOD technique is presented followed by a summary of the mathematical functions utilised with the MATLAB script. Furthermore, the images obtained for the schlieren image analysis are introduced and discussed.

3.2   TUSQ Facility

The University of Southern Queensland Hypersonic Wind Tunnel (TUSQ) consists of a Ludwieg tube with free piston compression heating that produces Mach 6 hypersonic air for approximately 200 ms (Buttsworth 2009). The long test flow duration is unique in comparison to other hypersonic testing facilities in Australia. This provides further ability to simulate unsteady aerodynamic problems (Buttsworth & Smart 2010).

The facility can be configured for two modes of operation: (1) a 16 m Ludwieg tube with free piston compression heating or (2) an atmospheric pressure, blow down to vacuum configuration. This mode of operation is suitable for various supersonic flow simulations. Typically, the facility is configured and operated as a free piston compression Ludwieg tunnel producing hypersonic low enthalpy flows from Mach 2 to Mach 7, replicating various aspects of hypersonic conditions. Figure 4. presents a schematic of the TUSQ facility. Annotated photographs from the high-pressure reservoir, nozzle section and test section are also provided in Figure 5.
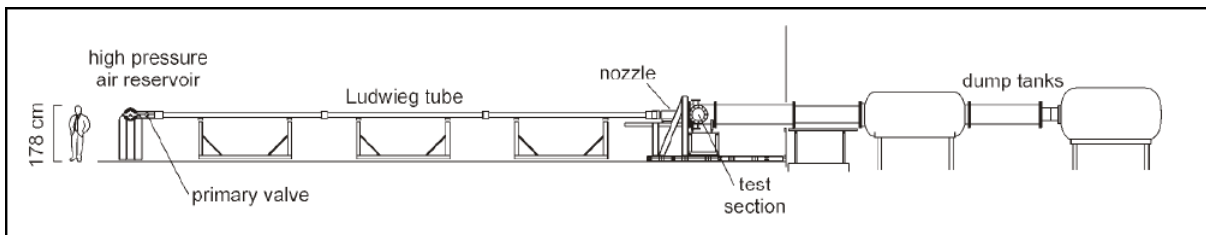
Figure 4. TUSQ facility (Buttsworth & Smart 2010)
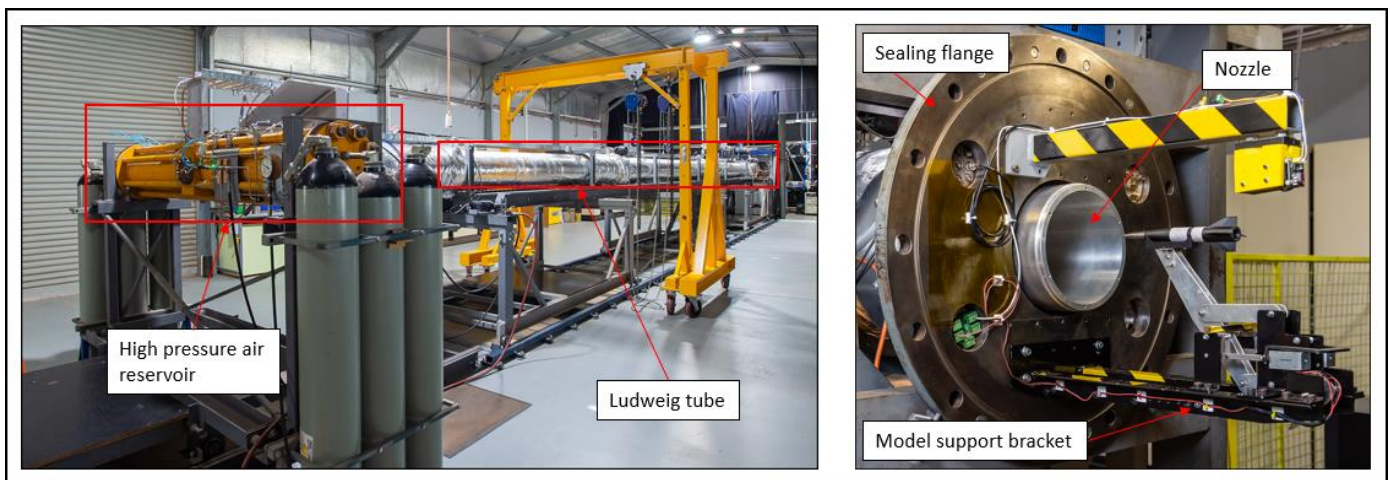
Figure 5. Annotated photographs of TUSQ components

For the Mach 6 flow used herein, the initial state of the facility consists of three gas regions: (1) the high-pressure reservoir of 3 MPa, (2) the barrel which contains air initially at 94 kPa at ambient temperature and (3) the nozzle, test section and dump tanks with a pressure < 1 kPa. A piston with a mass of 340 g is positioned downstream of the primary release valve and a Mylar diaphragm provides separation of the barrel from the nozzle inlet. Table 1. lists the properties of the fundamental components of the TUSQ facility.

Table 1. Fundamental components of TUSQ

Component	Characteristic
Air reservoir	Volume = 350 L
Primary ball valve	Ø27.6 mm
Nylatron piston	*m = 340 g*
Barrel	Ø130 mm, L = 16 m
Test section	Ø600 mm, L = 830 mm
Dump tanks	V = 12.5 m^3

A run commences by a controlled opening of the pneumatic ball valve. Jones et al. (1973) found that opening the primary valve slowly limits the magnitude of piston oscillations that can onset oscillations of the barrel pressure within the compression phase. Following the release of the high-pressure air, the piston is forced along the barrel tube, compressing the gas within it. The compression will continue until the 100 μm Mylar diaphragm located at the entry to the nozzle ruptures. The pressure in the tube is approximately 1 MPa at the point of rupture. After the rupture of the diaphragm, the gas accelerates through the nozzle and enters the test section. The barrel pressure measurement is achieved using a PCB 113A03 piezoelectric pressure transducer located upstream of the nozzle entrance. This transducer is amplified and converted using a Kistler type 5015 charge amplifier.

A cross section of the Mach 6 nozzle shown in Figure 6 provides an appreciation of the geometry and shows the pressure transducer mounted 225 mm upstream of the nozzle entrance for barrel pressure measurement.
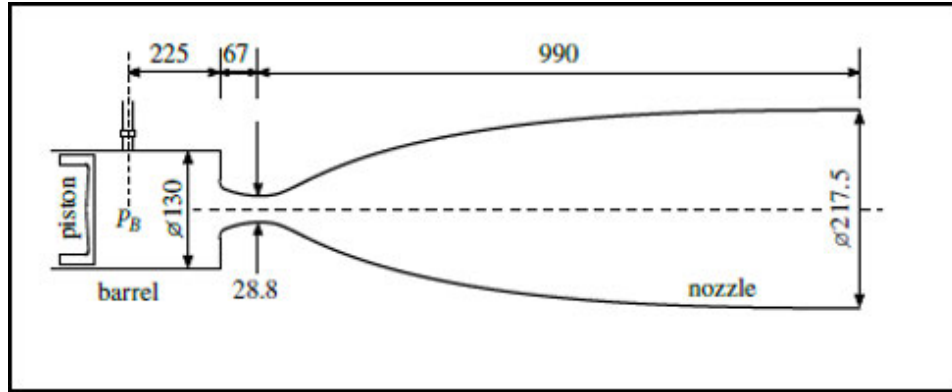
Figure 6. Cross section of the Mach 6 nozzle (Birch et al. 2018)

A trace for the typical barrel pressure is displayed in Figure 7. The trace is configured that t = 0 s is at the point of diaphragm rupture. The gradual opening of the valve is shown from ~ -1100 ms. This accelerates the piston, compressing the test gas. It is noted that once the primary valve is fully open, the approximate rate of pressure increase is 1.41 MPa/s.
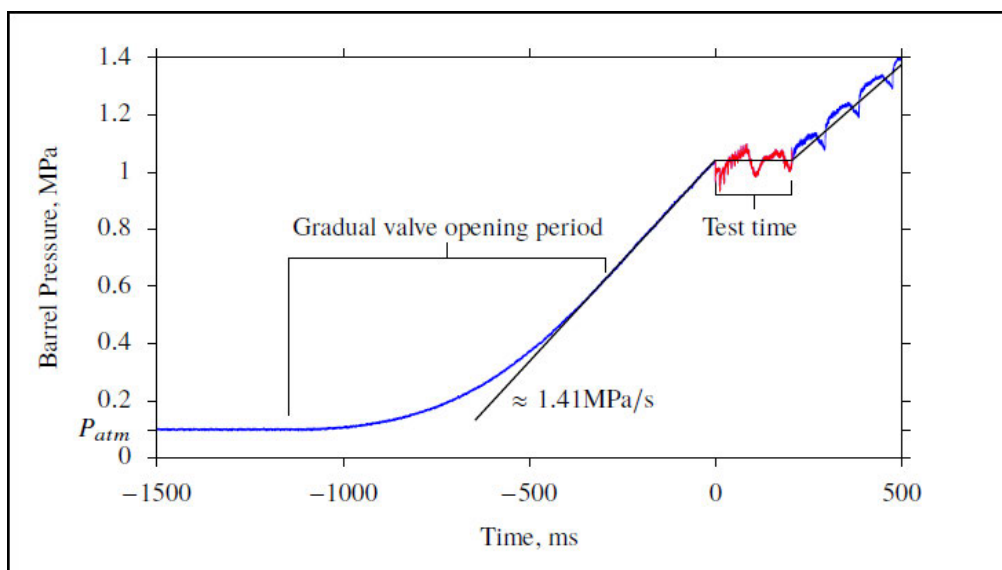
Figure 7. Barrel pressure based on historical data (Birch 2019)

3.3   Model Geometry

The instabilities present within the boundary layer of a 7-degree half angle precision machined cone have been investigated using SPOD. The cone is mounted to the model support bracket with a zero angle of attack in the hypersonic wind tunnel facility (TUSQ) located at the University of Southern Queensland, Toowoomba. A three-dimensional concept model was constructed by the staff at TUSQ. The Author was tasked with the manufacturing management of the cone. This responsibility included alteration to the design and drafting to suit manufacturability, material procurement, machining of components and final assembly. Workshop drawings are shown in Appendix E

A 7° half angle cone has been manufactured in three sections. These consist of nose tip, intermediate frustrum and the rear frustrum. A three-dimensional representation of the model is shown in Figure 8. The author acknowledges that the concept design of the 7° half angle cone was by others however, the author was responsible for the engineering design for manufacture, material procurement, machining and final assembly of the components.
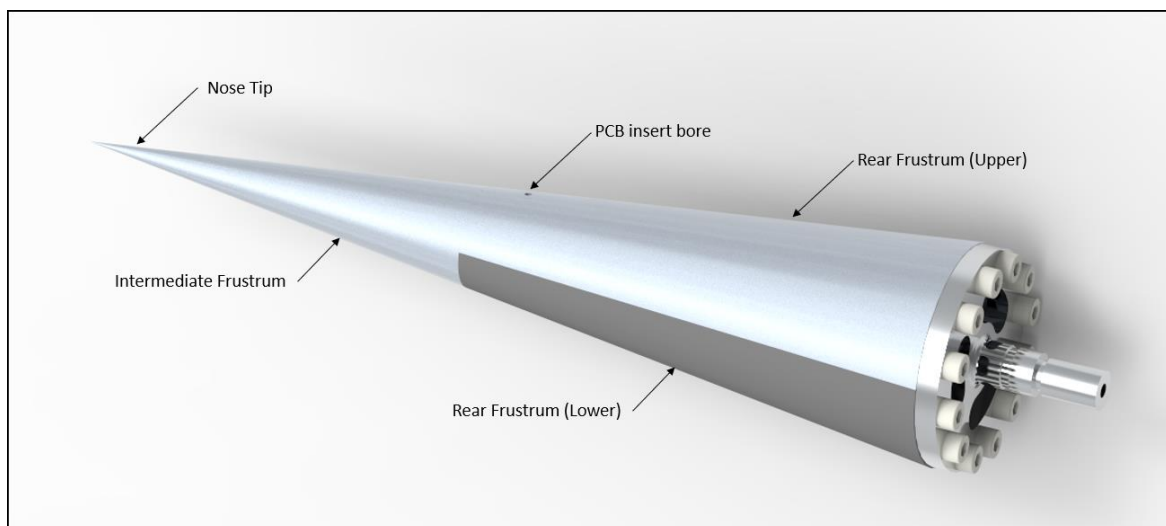
Figure 8. 7° half model cone representation

Four approximately 75 mm long nose tips were machined from 630 grade stainless steel with a common taper, counterbore and a screwcut internal thread for mounting to the intermediate frustrum. The final machining of the nose tips consisted of no radius, 0.05 mm radius, 0.1 mm radius and 0.2 mm radius. Figure 9 shows a comparison of each radius on a sharp nose tip at a scale of 20:1.
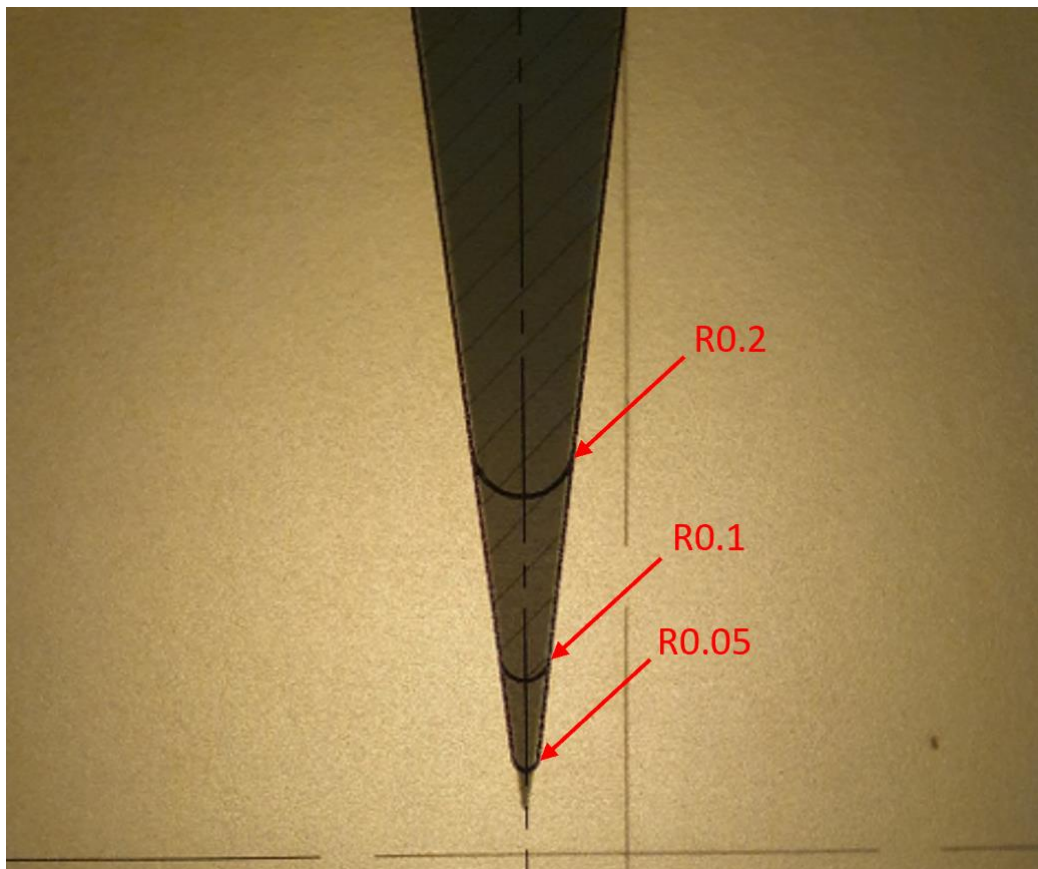
Figure 9. An example of the 0.05 mm, 0.1 mm and 0.2 mm radius at a scale of 20:1

This finish was achieved on a Kellenberger UR 175/1000 CNC cylindrical grinding machine. The intermediate frustum was machined from 630 grade stainless steel with an external thread to suit the nose tip and an internal thread and counterbore to suit the rear frustum with an approximate length of 110 mm.

A fixture was manufactured to mount the intermediate frustum to allow the taper to be machined +1 mm diametrically. The final machining to finished size was carried out as an assembly. Two mating sections are assembled for the rear frustum.

The upper section is machined from 630 grade stainless steel and the lower section is machined from black Acetal. The upper and lower sections were machined cylindrically. The internal profile consists of stepped counterbore sections that allow for cable access and fitting of the PCB inserts.

A fixture was manufactured to support the upper and lower sections. This allowed the individual sections to be machined in half allowing the PCB insert pockets and M3 tapped mounting holes to be machined into the upper section. This process was carried out on a Mazak 300IV Integrex CNC Lathe. The final operation involved assembling the model, including the PCB inserts. The assembly was mounted to a final operation fixture ensuring concentricity to the finish ground nose tips and then finish turned. This ensured a smooth transition between mating surfaces, eliminating inconsistencies within boundary layer analysis. Figure 10 shows a cross section of the cone that includes the field of view for the schlieren imaging that is presented in this work is marked with a red dashed rectangle. An annotated image of the completed machined 7-degree cone is shown in Figure 11.
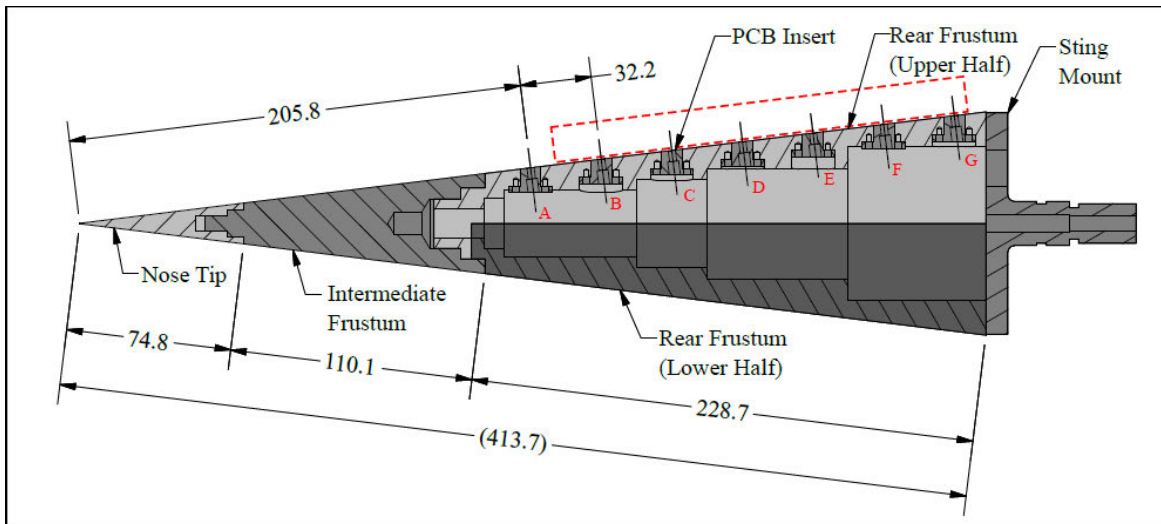
Figure 10. Cross section of model (Webb et al. 2022)
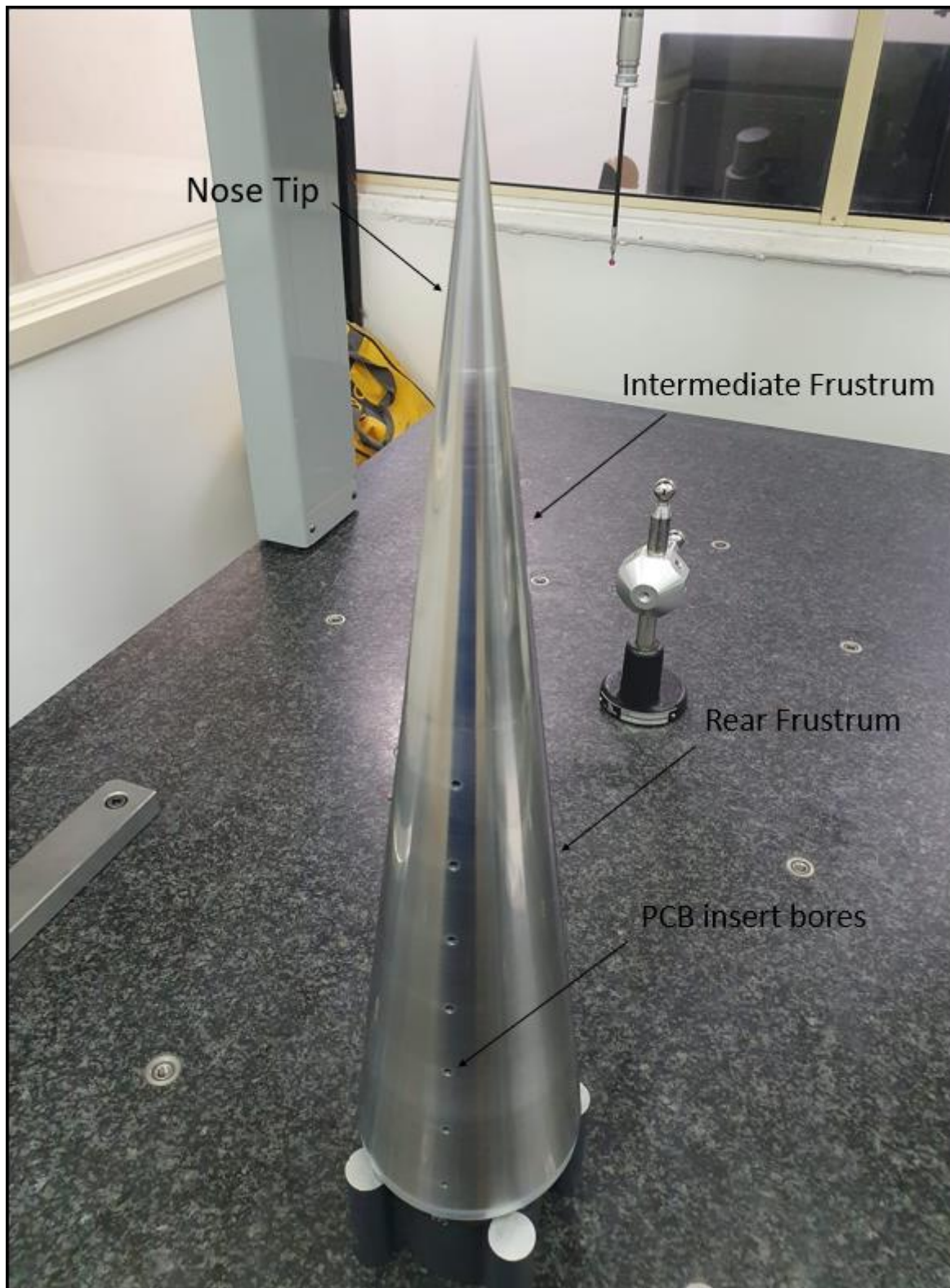
Figure 11. Image of the finished machined 7-degree cone with annotated components

All experiments for this study used the 0.2 mm radius tip nose tip. PCB132B38 sensors were mounted perpendicular to the surface of the cone and are installed with approximately 32 mm centres.

The pressure sensors were installed in positions D – G for the experiment for which the 450,000 fps schlieren imagery is available. Later testing with a complete suite of sensors was completed. However, the schlieren imagery from these tests could not be recorded as the high-performance high-speed camera was no longer on loan.

3.4   Experiment Design

The schlieren system utilised in this experiment was configured in a z-type arrangement. A schematic of the schlieren configuration is shown in Figure 12. The schlieren system arrangement at TUSQ consists of five mirrors. The mirrors are: three planar; and two on-axis parabolic mirrors with 2040 mm focal length. A knife edge, light source and a high-speed camera are included in the configuration. The laser used in this experiment is a Cavitar CAVILUX UHS ultra high-speed illumination smart laser. The monochromatic light output has a continuous operation duty cycle of 3% however, to achieve the 450,000 fps (20 ns exposure) required in this study, the duty cycle was exceeded for 6 ms followed by the laser being shut down to prevent failure due to excessive heat. This short exposure time eliminates motion blur effects in the flow. For example, a feature moving at 1 km/s (approximately the Mach 6 free stream velocity) moves only 20 micrometers in 20 ns. This performance is essential for the application of image processing techniques such as SPOD.

The high-speed camera was a Phantom TMX 7510 on a one-day loan from Adept Turnkey. The camera was used to capture the images at a rate of 450 000 fps with a resolution of 1280 x 128 pixels. The wall-normal density gradients were captured by positioning the knife edge and camera parallel to the surface of the upper section of the model (Webb et al. 2022).
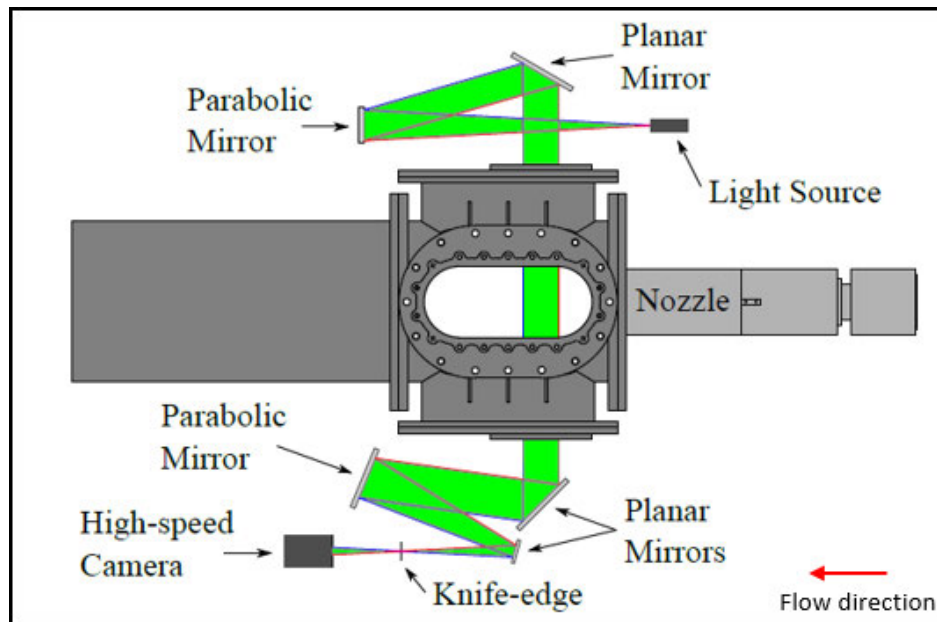
Figure 12. Representation of the schlieren system (Webb et al. 2022)

3.5 Schlieren Image Analysis

A set of images obtained from run 1229 have been obtained and reviewed for the SPOD analysis. A representative schlieren image from the 7-degree angle cone experiment is shown in Figure 13. Some features of interest have been annotated, including direction of flow, an observed rope like structure and the separation region.

Figure 13. Annotated schlieren image of the cone

Small areas of turbulence are observed in a variety of sizes however the boundary layer remains predominantly laminar. The transition from the laminar boundary layer flow to spots of turbulence is noticed to be in a transitional region of flow as no consistency in the flow was observed. However, rope like structures were observed in the laminar boundary layer. This characteristic is of second mode instabilities. This observation was also inconsistent of a repeatable pattern. Therefore, statistical and time-windowed methods are often used for analysis.

Figure 14 shows a sequence of schlieren images captured in the 7-degree cone experiment. The images represent a snapshot of the motion of the fluid flow and boundary layer interaction. It is observed that the laminar boundary layer dissipates where a turbulent spot emerges as the flow separates. This feature is observed to travel as a system although, as noted previously, in an inconsistent form.
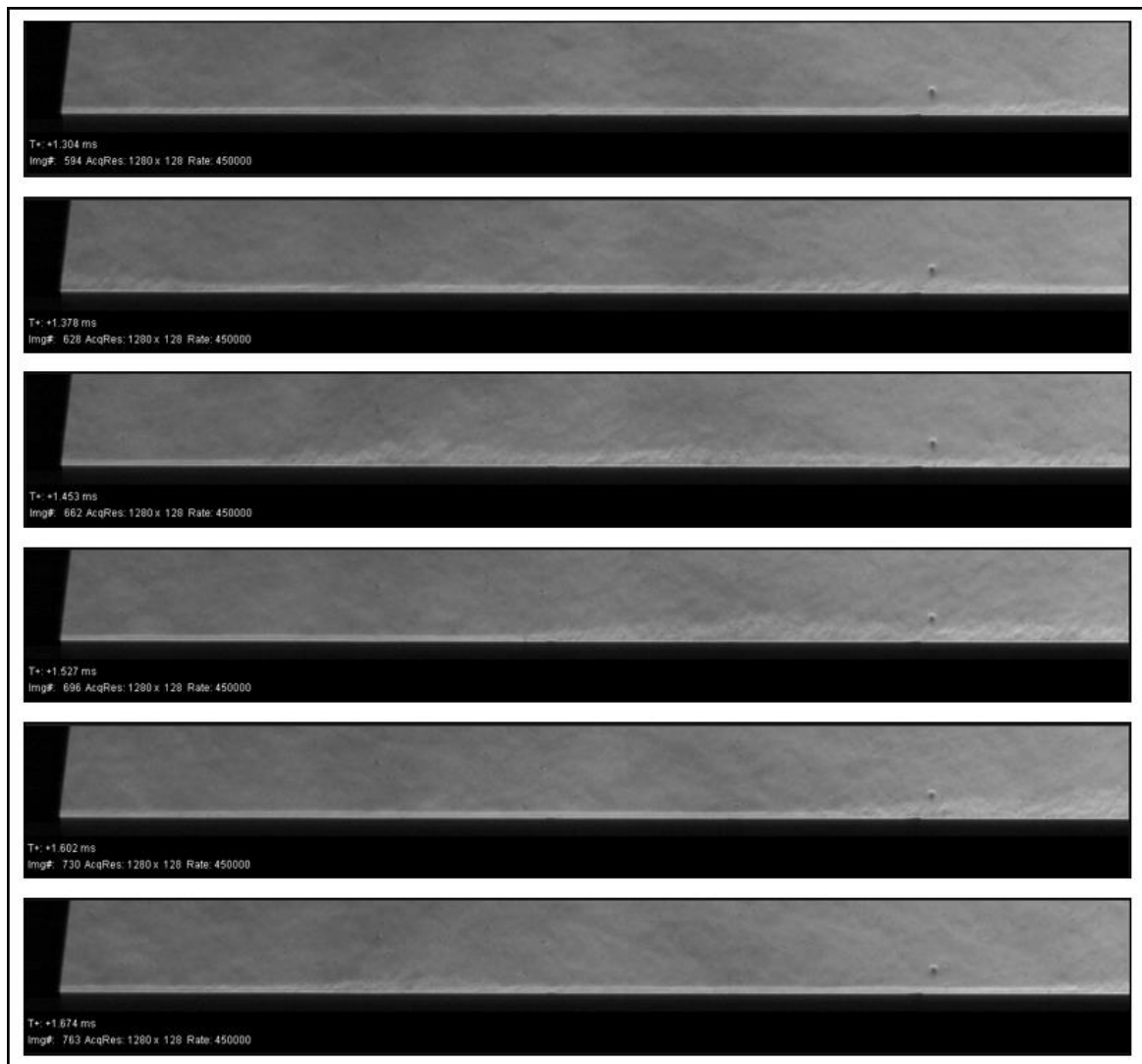
Figure 14. Sequence of images displaying the boundary layer motion

3.6   SPOD Technique

SPOD is an analysis tool that provides a common connection with respect to POD and DMD. The SPOD technique distributes flow data into modes much like the POD method however, SPOD includes the decomposition of the cross-spectral density tensor. Therefore, modes each oscillate at a singular frequency. POD results in modes that are spatially coherent where, SPOD results in modes that represent evolving coherently structures in time and space. Due to the uncorrelated frequency components of the Fourier transformation, the time dependency is retained (Towne et al. 2018).

The MATLAB script used for the SPOD technique in this research utilises the SPOD function code produced by Towne et al. (2018). The core of this function is based on a fast Fourier transform known as the Welch method, averaging the data over multiple realisations of the flow (Towne et al. 2018). A schematic depiction of Welch's method for the estimation of SPOD modes is shown in Figure 15.
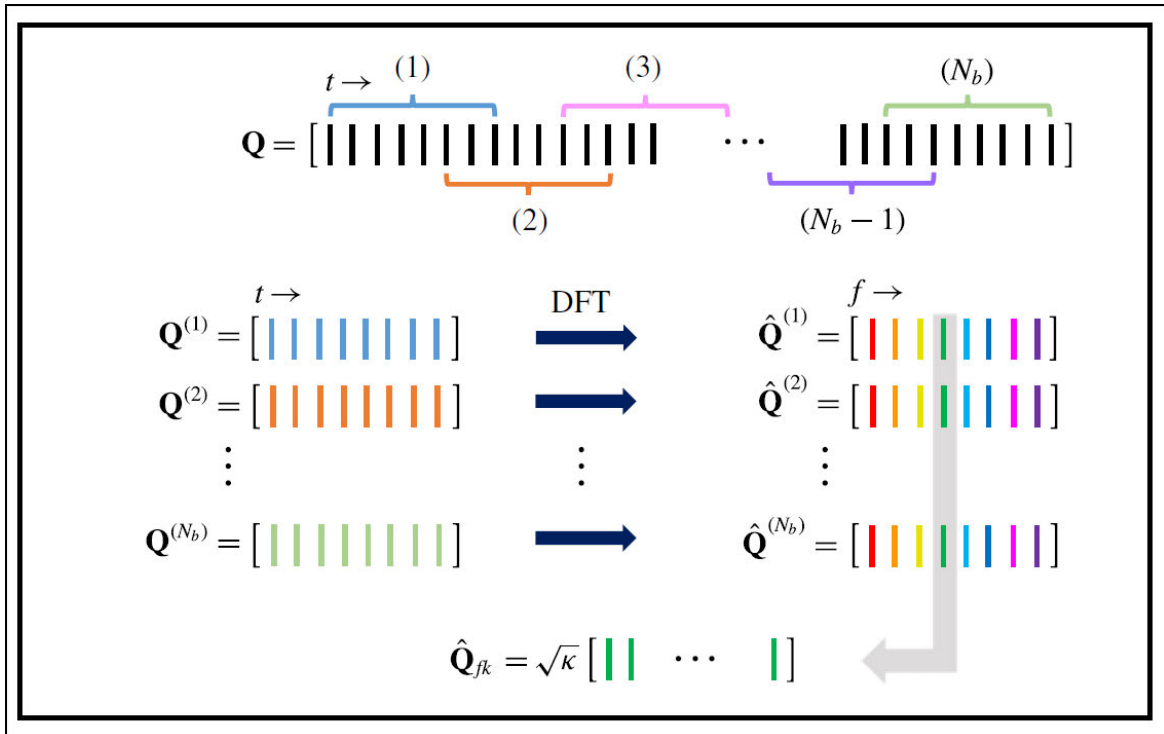
Figure 15. Schematic depiction of Welch's method (Towne et al. 2018)

This can be represented further by compacting into a data matrix (Towne et al. 2018).

$$\mathbf{Q} = [\mathbf{q}_1, \mathbf{q}_2, \ldots, \mathbf{q}_k, \ldots, \mathbf{q}_M] \in \mathbb{R}^{N \times M}$$

Equation 3

Where, $\mathbf{q}_k$ is a representation of the instantaneous state of $\mathbf{q}(x, t)$, M is the equally spaced time instances. The data set is partitioned into a set of smaller blocks that can overlap. The blocks are shown as N_b number of blocks and, N_f for the quantity of snapshots captured in each block. This is shown mathematically in Equation 4.

$$\mathbf{Q} = \left[\mathbf{q}_1^n, \mathbf{q}_2^n, \ldots, \mathbf{q}_k^n, \ldots, \mathbf{q}_{N_f}^n \right] \in \mathbb{R}^{N \times N_f}$$

Equation 4

Where, $\mathbf{q}_k^n$ is the kth entry in the nth block. Next, the discrete Fourier transform (DFT) is calculated for each block. This is achieved by computing a fast Fourier transformation.

$$\widehat{\mathbf{Q}}^n = FFT(\mathbf{Q}^n) = \left[\widehat{\mathbf{q}}_1^n, \widehat{\mathbf{q}}_2^n, \ldots, \widehat{\mathbf{q}}_k^n, \ldots, \widehat{\mathbf{q}}_{N_f}^n \right]$$

Equation 5

Where, $\widehat{\mathbf{q}}_k^n$ represents the Fourier component at the kth discrete frequency, f_k within the nth block.

Furthermore, arranging the Fourier coefficients at frequency f_k, a new compact data matrix can be written.

$$\widehat{\mathbf{Q}}_{fk} = \sqrt{k} \left[\widehat{\mathbf{q}}_k^{(1)}, \widehat{\mathbf{q}}_k^{(2)}, \ldots, \widehat{\mathbf{q}}_k^{(N_b)} \right] \in \mathbb{R}^{N \times N_b}$$

Equation 6

Where, $k = \frac{\Delta t}{s N_b}$ and $s = \sum_{j=1}^{N_f} w_j^2$. The nodal value of the window function is used to control inconsistency of non-periodicity. This is known as scalar weights, w_j^2 (Cottier 2019).

The estimated cross-spectral density tensor can be written at frequency f_k,

$$S_{fk} = \widehat{\mathbf{Q}}_{fk}\widehat{\mathbf{Q}}_{fk}^{*}$$

<div align="right">Equation 7</div>

Convergence of this estimate is achieved when the number of blocks N_b and snapshots within the block N_f increase simultaneously. This reduces the infinite-dimensional eigenvalue problem to an N x N matrix eigenvalue problem. Spectral decomposition decomposes the cross-spectral tensor where the SPOD modes can then be calculated. SPOD modes are shown to be an optimal research analysis tool due to efficiency in the identification of flow structure that evolves coherently in time and space (Towne et al. 2018).

3.7   PCB Inserts

The baseline measurement for comparison to the SPOD study was achieved by measuring the pressure fluctuations of four sensors mounted normal to the cone surface. The sensor model is PCB132B38 and have a working capacity from 11 kHz to 1 MHz. The sensors were installed in positions D-G for the present SPOD analysis work. PCBs serve an excellent tool for performance reference and comparison in this work. These sensors have become a standard for second mode amplitude measurement and have performed in hypersonic wind tunnels worldwide (Marineau et al. 2018)

Chapter 4

Results

4.1   Chapter Overview

Results from the power density spectrums of two TUSQ runs are presented in this chapter. Measurements have been taken by a suite of PCBs mounted to the surface of the upper rear frustrum of the 7-degree cone. A SPOD analysis has been conducted using schlieren visualisation. Discussion of the comparison between the methods identifies effects that may have impacted the data.

4.2   PCB Data

4.2.1   TUSQ Run Overview

The 7-degree half cone model has been analysed in TUSQ with two configurations. The configuration of the first run, 1229 consisted of four sensors assembled in positions D, E, F and G. This analysis included utilising the high-speed camera, Phantom TMX 7510 on loan from Adept Turnkey. The high-speed camera captured the schlieren data of interest for the SPOD analysis. The configuration of the second run, 1374 consisted of seven sensors assembled in positions A, B, C, D, E, F and G. TUSQ run configurations have been tabulated in Table 2. PSD analysis was obtained and observed for TUSQ run 1229 and 1374 for this study and used as a comparison for the schlieren data for SPOD analysis. Run 1374 included the full pressure sensor suite therefore, this run was considered first.

Table 2. TUSQ runs for 7-degree half cone model

	Inserts							Available data flow duration for schlieren (ms)
	A	B	C	D	E	F	G	
TUSQ Run 1229 PCB analysis				•	•	•	•	21
TUSQ Run 1374 PCB analysis	•	•	•	•	•	•	•	21
TUSQ Run 1229 schlieren data of interest for SPOD analysis				•	•	•	•	6

4.2.2   PSD analysis of TUSQ Run 1374

The raw signals of all PCBs installed for TUSQ run 1374 have been calibrated and the pressure graphed in Figure 16. The plot has been offset in the pressure fluctuation axis for clarity.

The PCB pressure provides an overview of quality and expectation of data obtained for further PSD analysis.
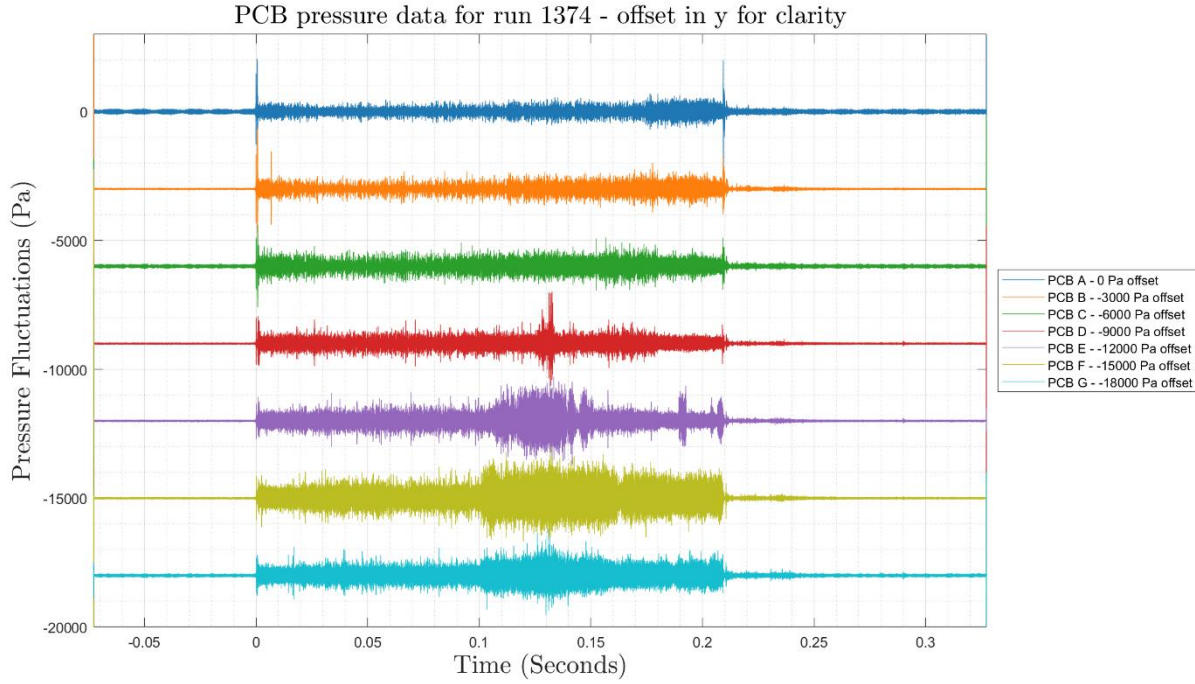
Figure 16. PCB pressure for complete run time of all PCBs for run 1374

A power spectrum density (PSD) analysis of run 1374 has been computed and shown in Figure 17. Additional PCBs were installed in the 7-degree cone for further analysis of the boundary conditions of the rear upper frustrum. The nomenclature of these PCBs is A through to G. The results have been windowed over the domain $T_0 = 10$ ms and a window length of time of 20 ms. Windowing of the data to a limited section of 10-30 ms of the run duration provides a longer time series than achieved with the 6 ms of schlieren data.

This longer duration window allows a clearer PSD plot due to the reduction of background noise and unnecessary peaks outside of the second mode interest of 200-300 kHz without sacrificing data fidelity as this extended period is still within the steady test flow period.

All PCBs displayed peaks between 200 and 300 kHz. Frequencies beyond 450 kHz are not related to the second mode instability. Further electrical noise is observed in the range of 700-850 kHz and 864 kHz AM radio frequencies.
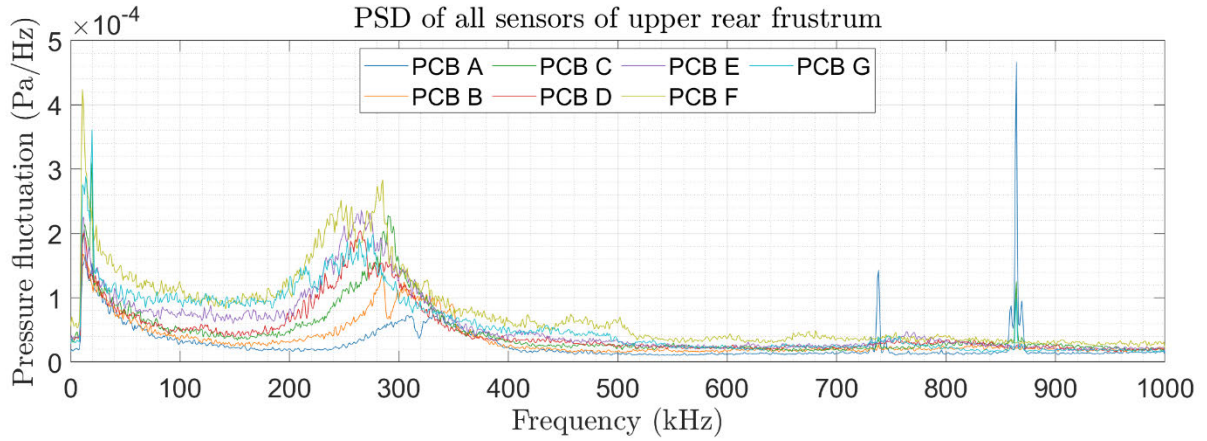
Figure 17. Power spectrum plot for 20 ms from domain t_0 =10 ms – TUSQ run 1374

Figure 18 shows a narrowed representation of the PCBs within the 200-300 kHz area of interest. Narrow peaks observed below 20 kHz are not consistent between the sensors. This inconsistency is caused due to electrical noise from the PCB wiring and strain relief. The observation obtained from analysis shows that the intensity increases along the cone. Each PCB observes an increase in intensity over the assembled 32 mm centres, confirming that the amplification of the second mode occurs spatially.

The second mode growth along the cone is identified by the increase of energy within the 200 – 350 kHz band. The peak energy frequency decreases with distance along the cone consistent with the second mode instability propagating in a boundary layer of increasing thickness.

There is recurrence between PCB A to PCB F however, PCB G observes a decrease in amplitude. This indicates a decay to turbulence in the region between PCB F and PCB G. Furthermore, the peak wavelength decreases along the surface of the cone as expected, as the boundary layer increases.
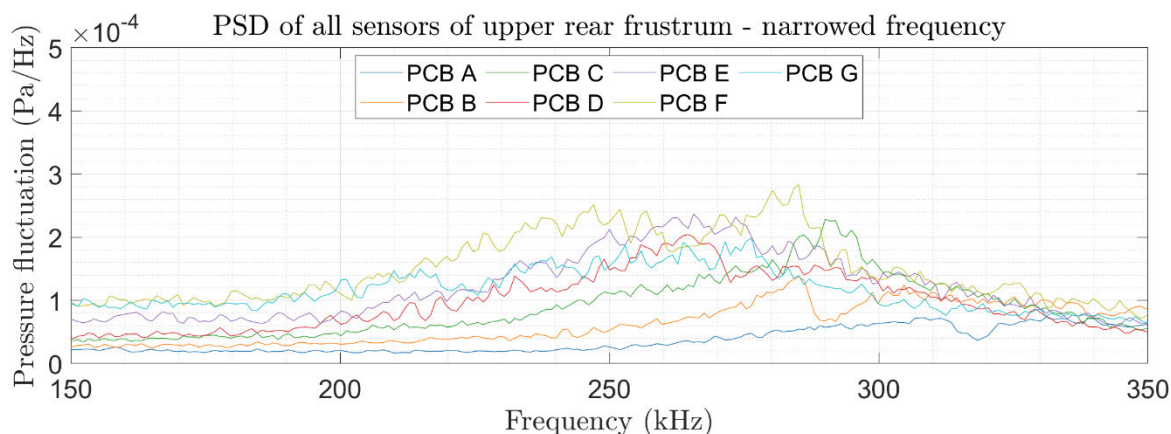
Figure 18. Power spectrum plot 20 ms from domain t=10 ms from run 1374 with narrowed frequency to area of interest

4.2.3 PSD analysis of TUSQ Run 1229

A spectrogram of PCB D over the complete flow time of the run is shown in Figure 19. This shows a representation of the frequencies observed over the run time. The annotation shows a greater power spectrum in the frequency 200-300 kHz. This complies with the expected second mode area of interest.
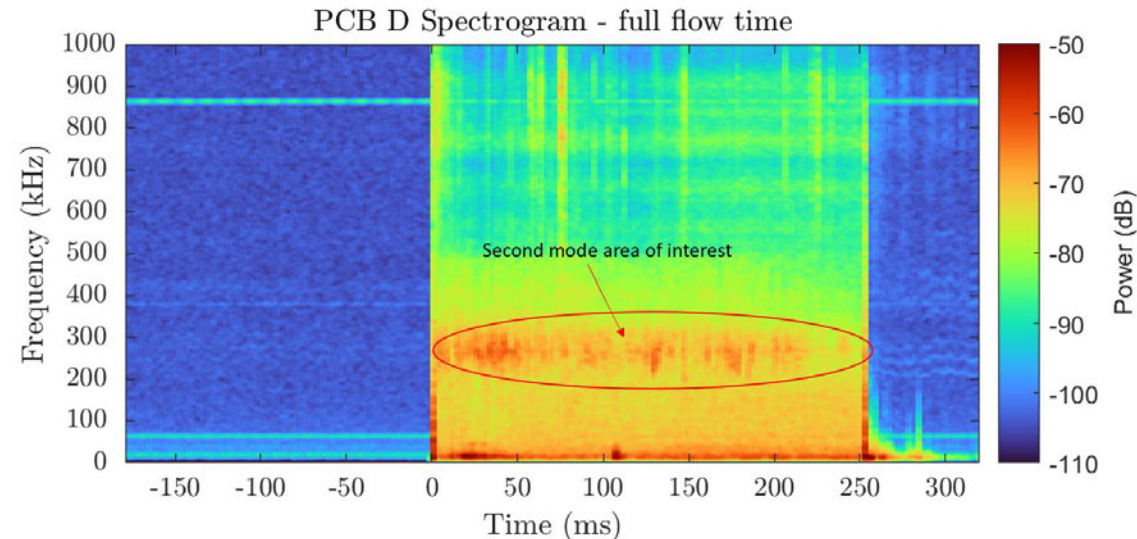
Figure 19. A visual representation of the spectrum of frequencies of the signal as it varies over the time of the run including annotation of the second mode region of interest for PCB D

The raw signals of PCB D to PCB G of TUSQ run 1229 have been calibrated using manufacturer supplied calibrations; and the barrel pressure for Run 1229 is shown in Figure 20. The plot has been offset in the pressure fluctuation axis for clarity. The complete barrel pressure plot is shown in Appendix H.

Sharp spikes in the plot are likely to be particulate effects. Spikes should be identified and masked form the PSD process as the step change can excite all frequencies. It is observed that PCB G experiences a large degree of amplitude noise from 150 ms. This is due to the nozzle Mach wave impinging on the cone surface. This region will be omitted from further analysis as it is a flow period not consistent with the schlieren images.
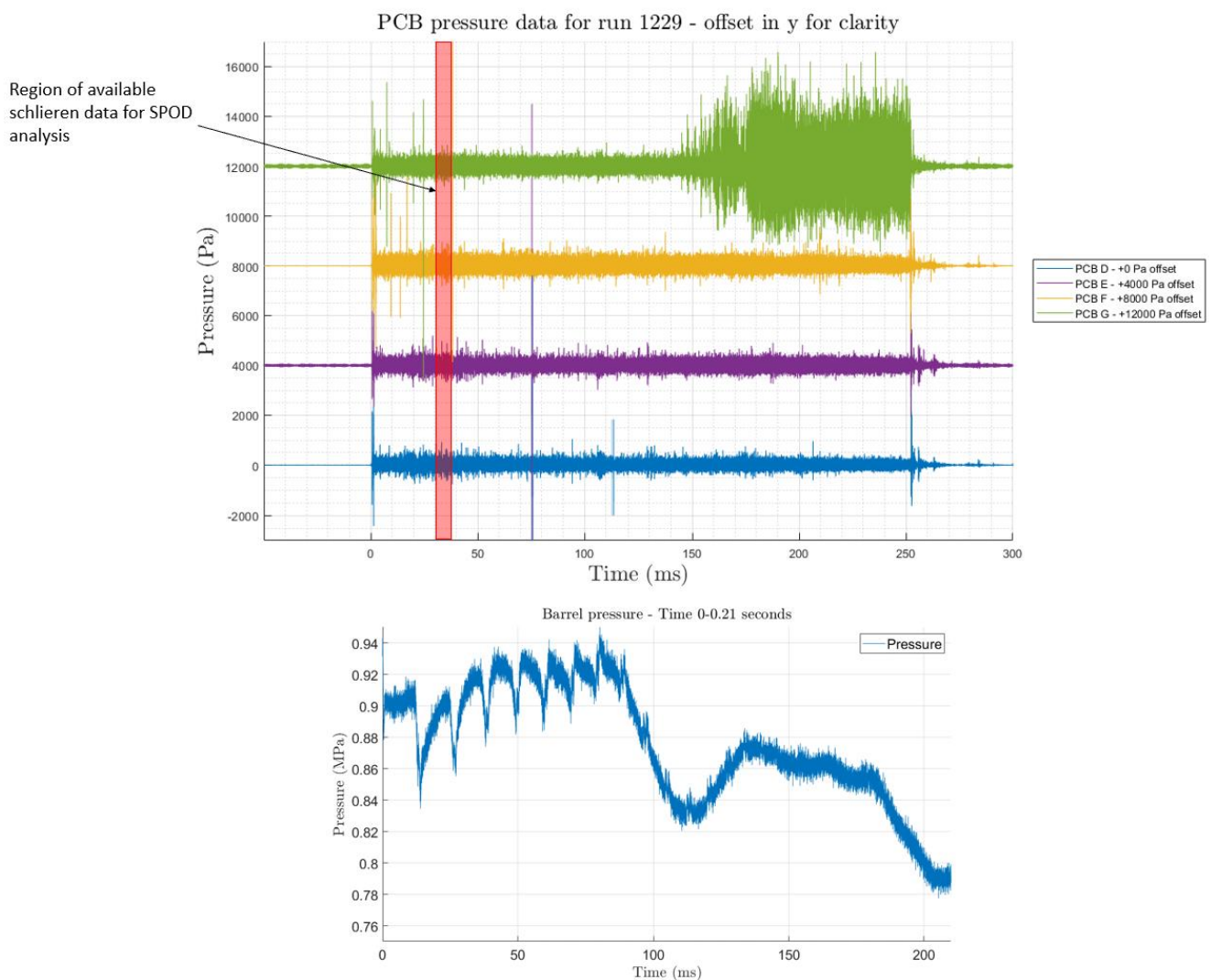
Figure 20. PCB pressure for complete run time of PCB D – PCB G (top) Barrel pressure for T = 0-0.21seconds from run 1229 (bottom)

A Baseline for the PSD measurements for TUSQ run 1229 was produced for PCB D to PCB G as shown in Figure 21. The prefow was analysed for 50 ms from T_0 = -120 ms. The global plot is shown in Figure 21 is on the same scale used to present the baseline pre-flow noise level to enable direct comparison of the flow-on and baseline states. As discussed in 4.2.2, increased spikes due to electrical noise is present beyond 700 kHz. Inconsistent narrowband peaks at < 200 kHz are observed due to electrical noise on the sensors however, the 200-300 kHz region shows a low level of amplification.
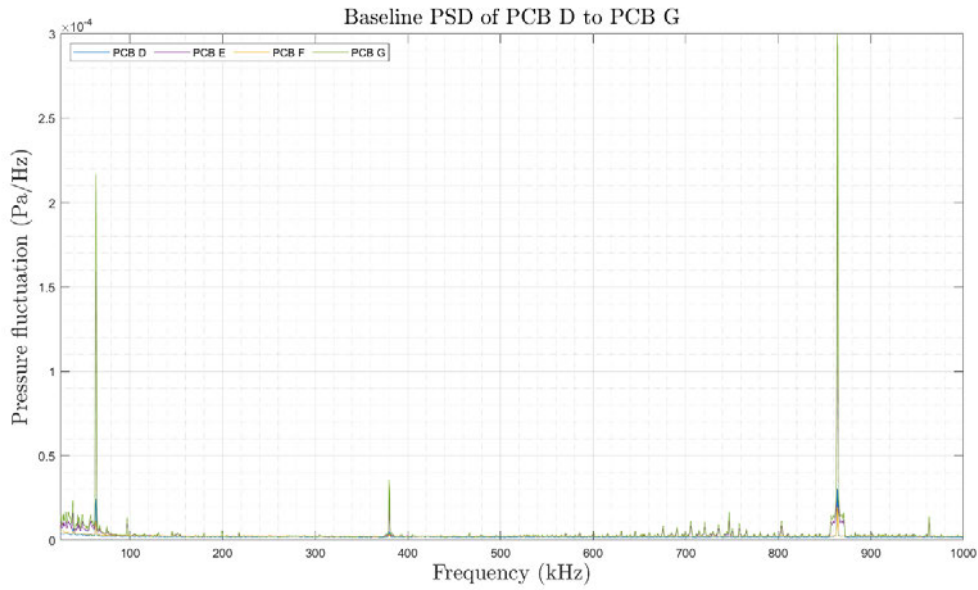
Figure 21. Global baseline for pre flow PSD for 50 ms duration where T_0 = -120 ms

A power spectrum density (PSD) analysis of run 1229 is shown in Figure 22. The observed run included four PCB sensors assembled in the 7-degree cone upper rear frustrum. The nomenclature of these PCBs is D through to G. The results have been windowed over the domain $T_0 = 10$ ms and a window length of time of 30 ms.

All PCBs displayed peaks between 200 and 300 kHz. As per section 4.2.2, frequencies beyond 450 kHz are not indicated as useful therefore, ignored. Further electrical noise is observed in the range of 700-850 kHz. This is potentially strain relief or poor shielding. However, 864 kHz is due to AM radio frequencies. The increased pressure fluctuation observed with PCB G shows consistency with Mach wave impinging on the cone surface as seen in the PCB pressure data shown in Figure 22.
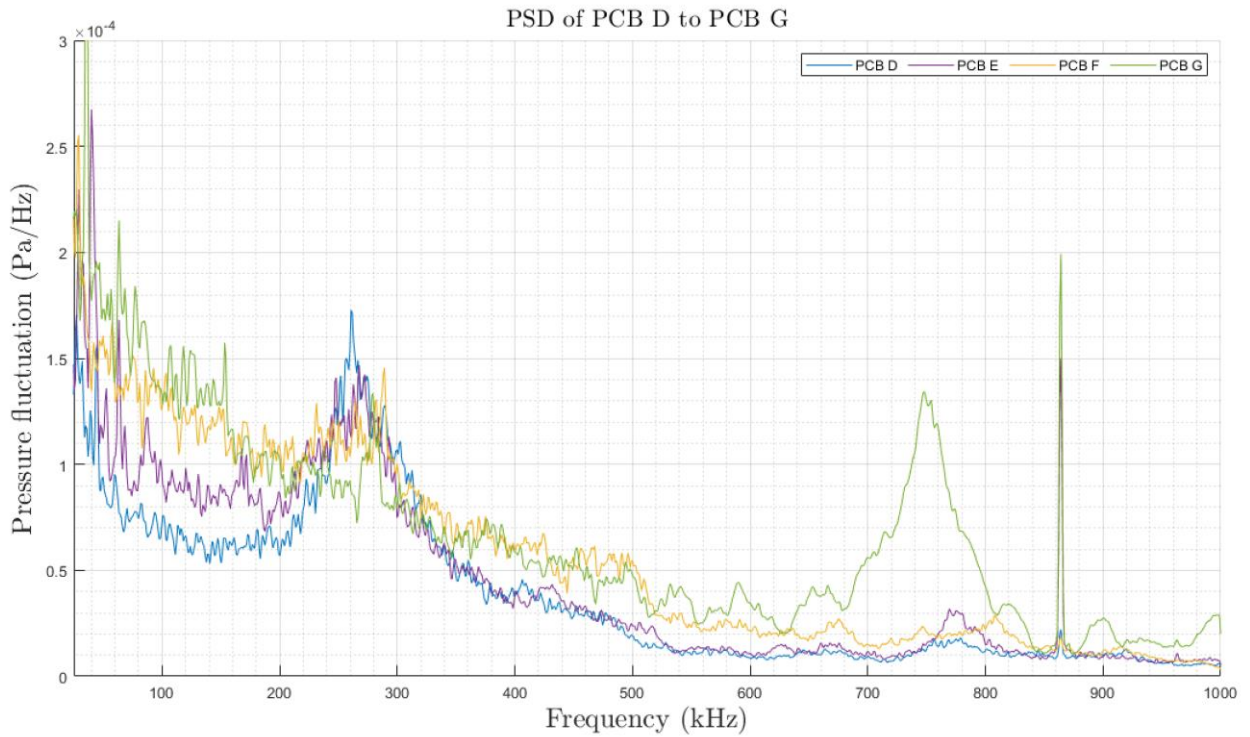
Figure 22. Power spectrum plot for 20 ms from domain t_0 =10 ms – TUSQ run 1229

A narrowed frequency plot showing greater clarity of the 200-300 kHz area of interest is shown in Figure 22. Electrical noise from the PCB wiring and strain relief shows narrow peaks below 20 kHz which are not consistent between the sensors. This shows consistency with the results observed in section 4.2.2, TUSQ run 1374. PCB D to PCB F shows spatial increases in intensity along the cone surface with the exception of PCB G, as this indicates a decay to turbulence within the region.
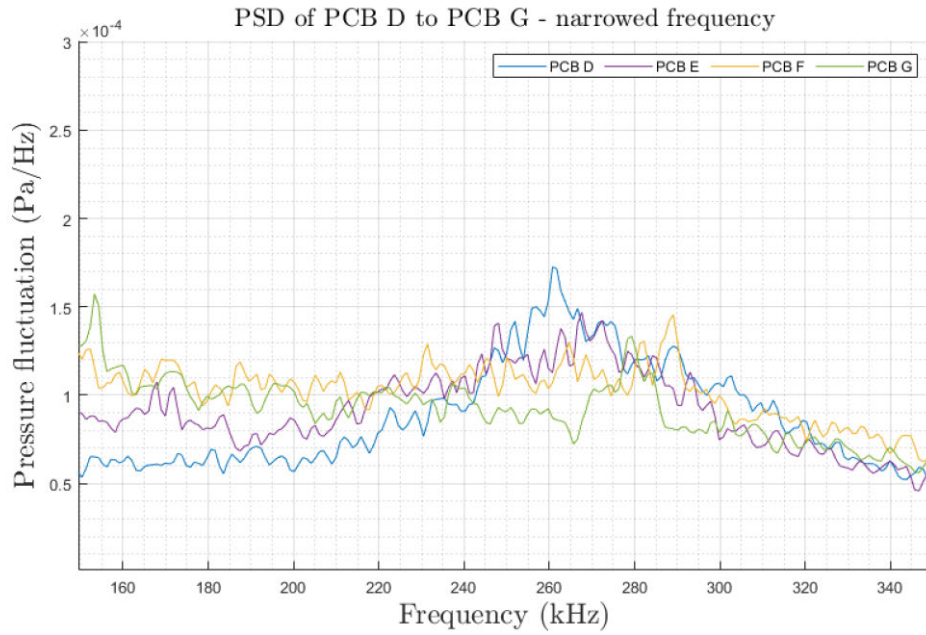
Figure 23. PSD plot 20 ms from domain t=10 ms from run 1229 with narrowed frequency

A PSD plot with a dB scale shown in Figure 24. This provides a clear comparision for the PSD for TUSQ run 1229 with the baseline for the facility. Providing a clear signal-to-noise indication (SNR). The baseline shows the average measurments of PCB D to PCB G from t = 10 ms to t = 30 ms. Clearly, there is sufficient signal above the baseline to enable surface pressure fluctuation measurements using PCBs.
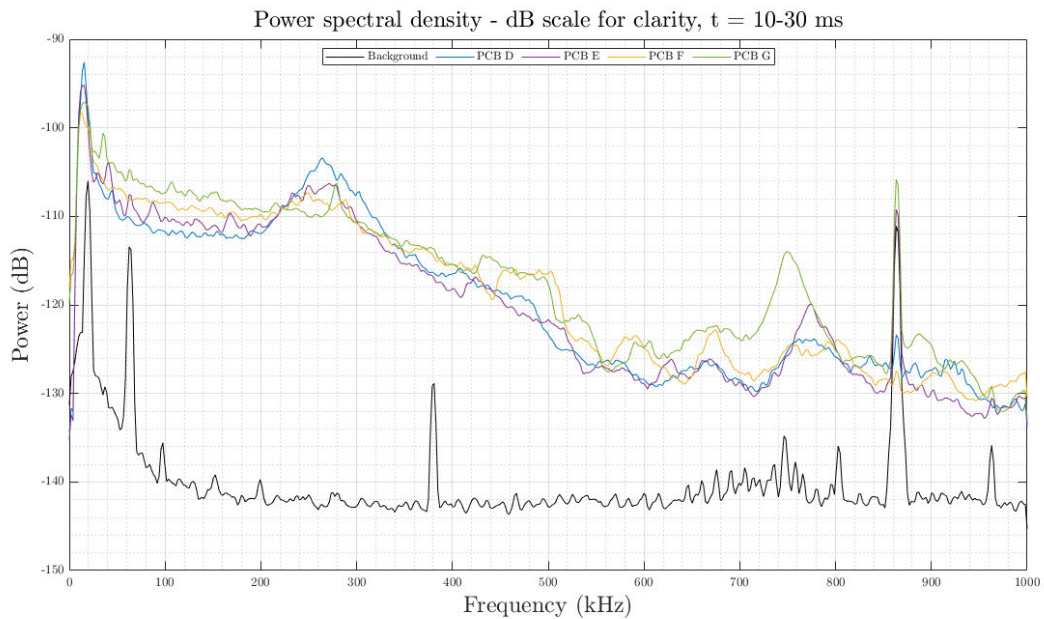
Figure 24. PSD plot on dB scale for clear signal to noise indication (SNR)

4.3   SPOD Analysis

4.3.1 SPOD energy spectra

The SPOD methodology by Towne et al. (2018) produces the SPOD modes as an eigenvector and the corresponding eigenvalues is the modal energy within the cross-spectral density matrix. SPOD modes are sorted in decreasing energy ensuring that the modes maintain the orthonormality properties. SPOD modes are arranged in an optimal format with respect to their energy. Therefore, the first SPOD mode is generally referred to as the optimal mode where is, the following modes are of lower energy and referred to as suboptimal modes.

Examination of the change in modal energy as a function of the frequency is presented by plotting the SPOD eigenvalues for each mode as a function of frequency resulting in a line graph of the SPOD energy spectra, as presented in Figure 25. The SPOD energy spectra plot asserts that dominant structures are not identified in the SPOD analysis. From the PCB data, an increase in modal energy at around 200 kHz is expected although not apparent. Figure 25. This is approaching the maximum frequencies which can be resolved from Run 1229 where the 450,000 fps schlieren video data is available. A small spike is observed at 191 kHz. This unknown feature will be discussed later in the report.
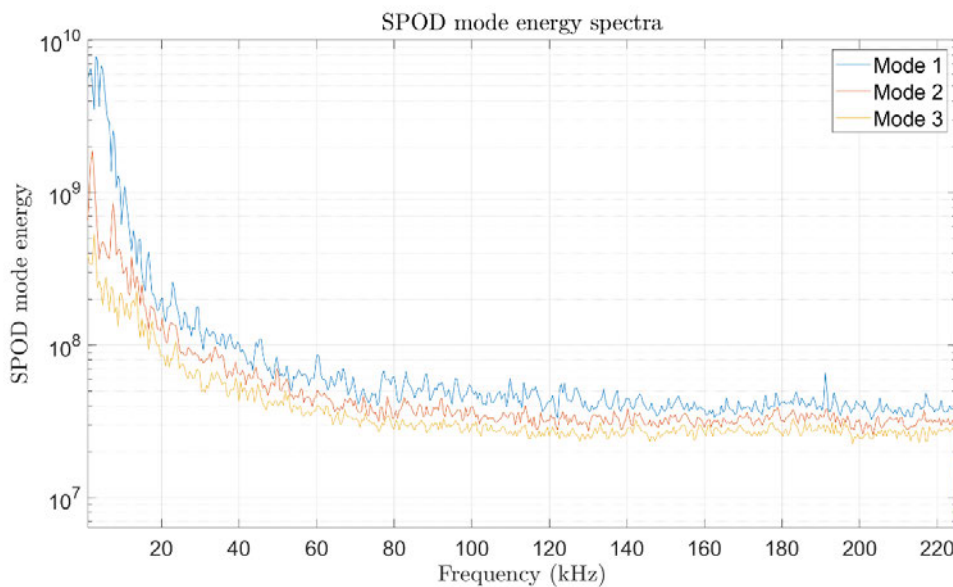
Figure 25. SPOD mode energy spectra plot

The schlieren apparatus in TUSQ is not calibrated. Calibration can be achieved although, it is not practical in the current environment due to uncontrollable conditions. However, structures can be observed in the SPOD spectra images.

The schlieren field of view for the SPOD analysis is shown in Figure 26. PCB D to G can be seen along the surface of the cone and have been annotated for clarity. Further analysis includes windowing the crop zone of the SPOD program to within the vicinity of each PCB and produce plots for these regions.
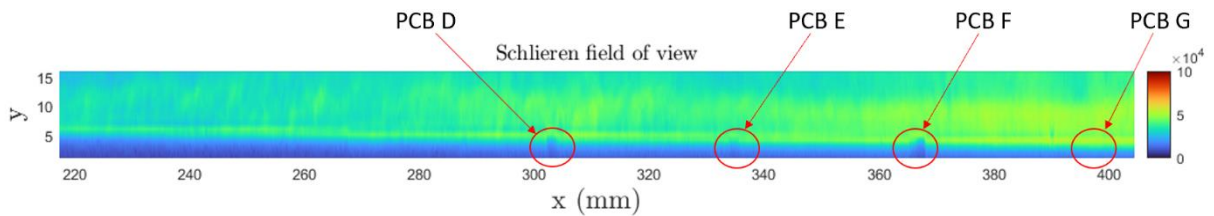
Figure 26. Schlieren field of view

The schlieren image has been windowed to the vicinity of each PCB as an alternative method for the SPOD analysis. Figure 27 shows the field of view that has been analysed post windowing by the crop zone function. This reduced and localised field of view was implemented to investigate if the PSD from SPOD could be improved and better spatially resolved.
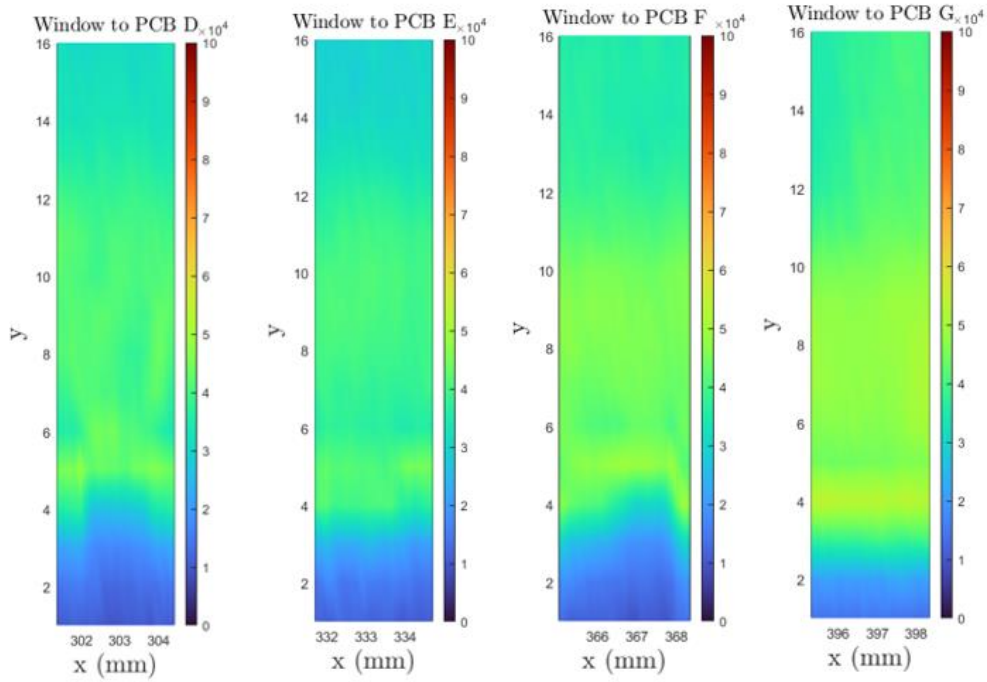
Figure 27. Field of view of the PCBs as a result of windowing

As shown in Figure 28-30, the SPOD energy spectrum exhibited no clear increase due to the second-mode instability, or any other flow feature. As the schlieren imaging was recorded at 450,000 fps, the maximum frequency which could be resolved from this data was 225 kHz, which is insufficiently high to resolve the entire energy spectrum containing the second mode as identified from the surface pressure fluctuation measurements. However, some increase at <200 kHz should be observed.
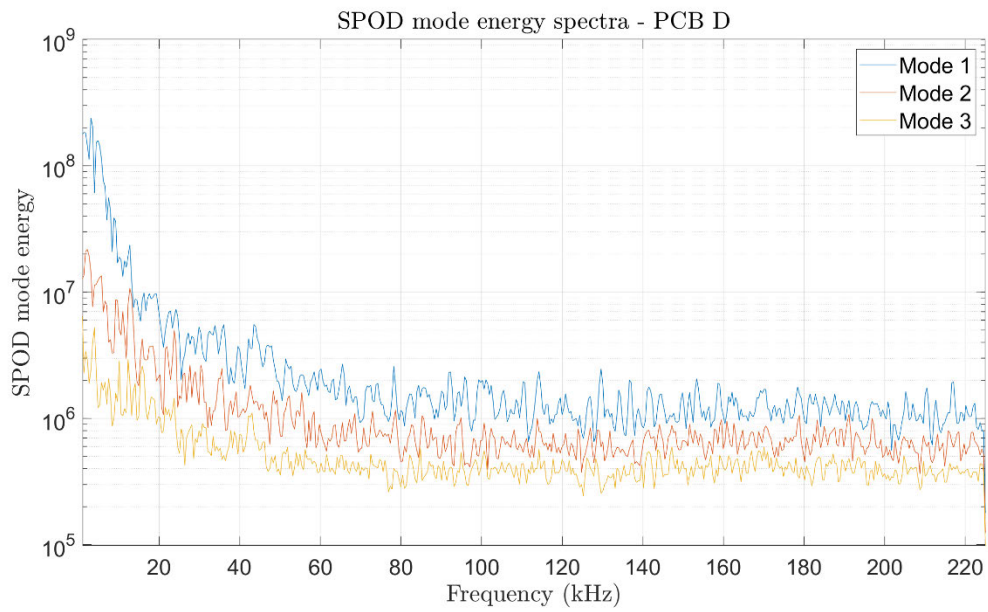
Figure 28. SPOD mode energy spectra plot vicinity of PCB D - cropzone = [600 95 20 15]
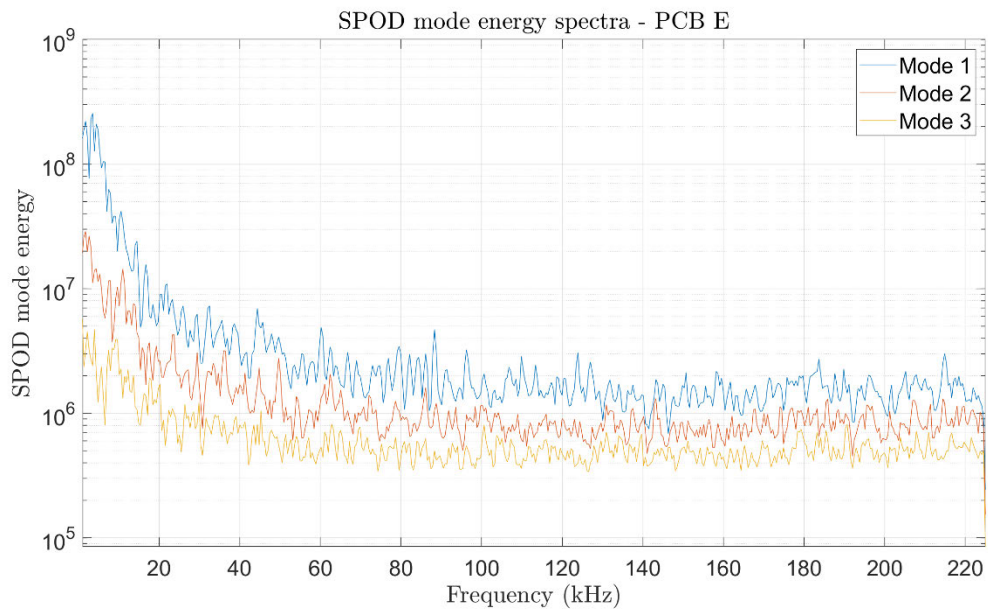
Figure 29. SPOD mode energy spectra plot vicinity of PCB E - cropzone = [800 95 20 15]
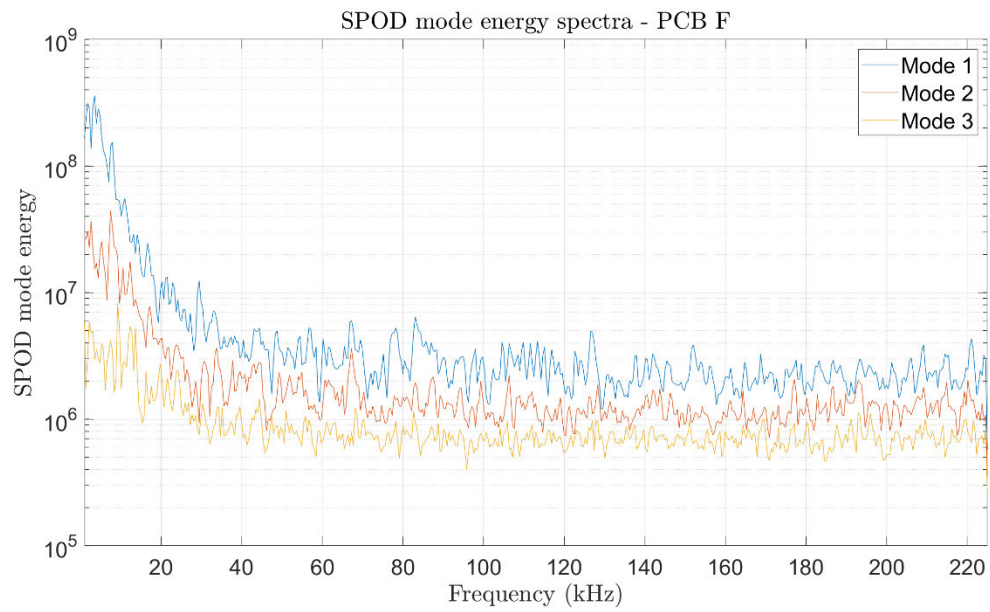
Figure 30. SPOD mode energy spectra plot vicinity of PCB F - cropzone = [1020 95 22 15]
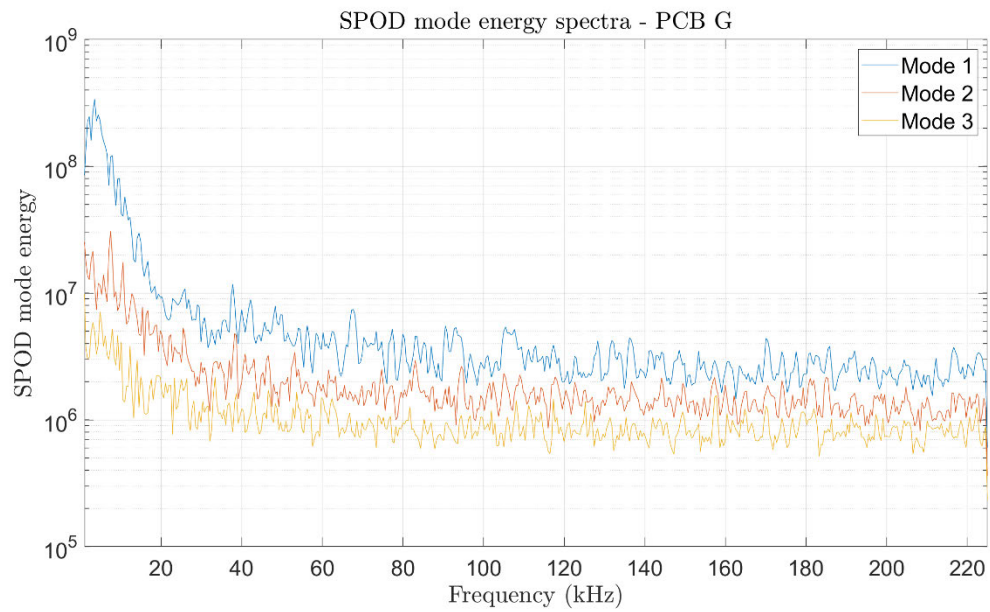
Figure 31. SPOD mode energy spectra plot vicinity of PCB G – cropzone = [1220 95 20 15]

4.3.2 Investigation of observed high frequency spike

A sharp increase in frequency is observed at 191 kHz however, a SPOD spectra plot as shown in Figure 32 of this failed to provide a conclusion for the spike. The plot shows that frequencies in the vicinity of 191 kHz do not experience an entire excited frame.
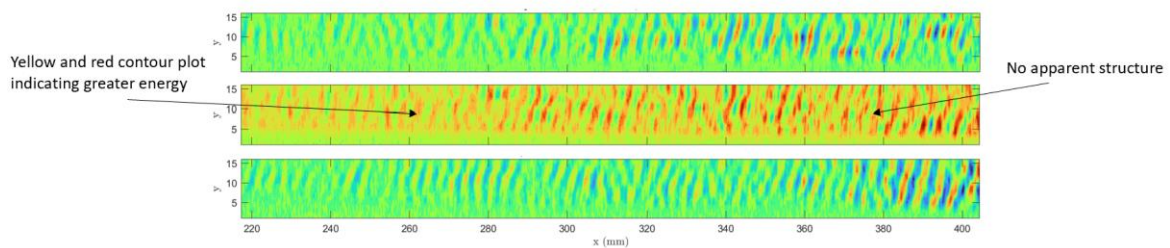
Figure 32. SPOD spectra image of 190 kHz (top), 191 kHz (middle) and 192 kHz (bottom)

The initial assumption of the interference is the result of switching frequency of an LED light within the lab. Pre-flow schlieren imaging concluded that the spike is evident prior to the run. Further analysis consisted of the application of a photodetector in the TUSQ lab. The results of this analysis showing the frequencies of lighting within the TUSQ lab is shown in Table 3.

Table 3. Photodector results in TUSQ

Frequencies within TUSQ	
69 kHz	
111 kHz	Potentially visible in SPOD analysis
136 kHz	Potentially visible in SPOD analysis
157 kHz	
204 kHz	
225 kHz	

It is reasonable to assume the 191 kHz would come from lighting previously in the lab that was replaced between the run and the identification of this feature however, further

explanation of the sharp spike could not be identified. The analysis concluded that this frequency is not flow related and further investigation would require an analysis of the test camera however, this is not within the scope of this study. Therefore, frequencies from this region are omitted in this report.

4.3.3 Background subtraction

A simple average background flow field subtraction method was performed in attempt to emphasise the boundary layer however, from the authors observation, this did not improve the clarity of the image. A SPOD mode energy spectra plot was generated for both conditions and is shown in Figure 33.
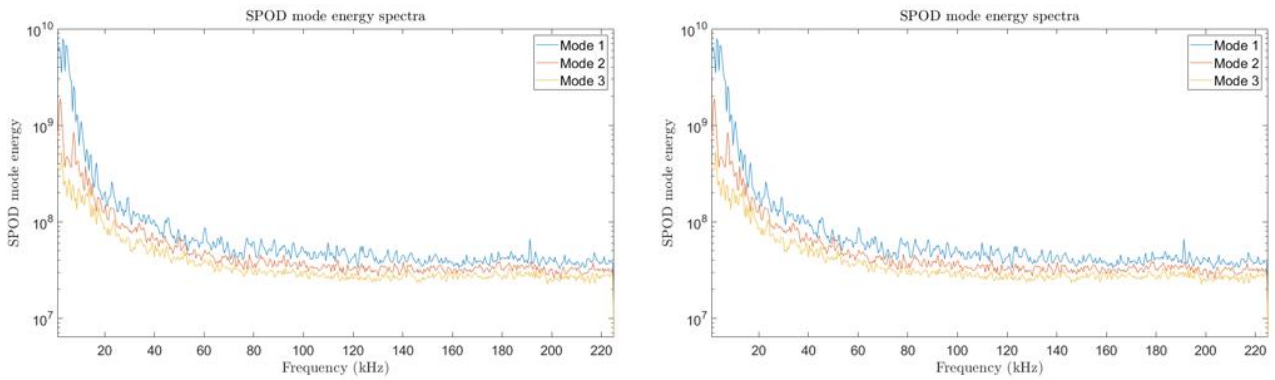
Figure 33. SPOD mode energy spectra plots with no background subtraction (left) and with background subtraction (right)

4.3.4 SPOD spectra images

Each mode within the second mode of interest was visualised by plotting a SPOD mode spectra image. This method proved as a reliable comparison to the SPOD mode energy spectra plots to confirm if structure was present within the schlieren images. On conclusion of the spectra image plots, it was confirmed that a clear rope like structure in the schlieren image was observed and present. This provides the suggestion that second mode instabilities within the boundary layer do exist.

Wavepacket convection velocity, frequency and wavelength structure angle is generally utilised to provide further classification of second mode instability however, this was not in the scope of this research. An example of the observed structures at various frequencies are shown in Figure 34.
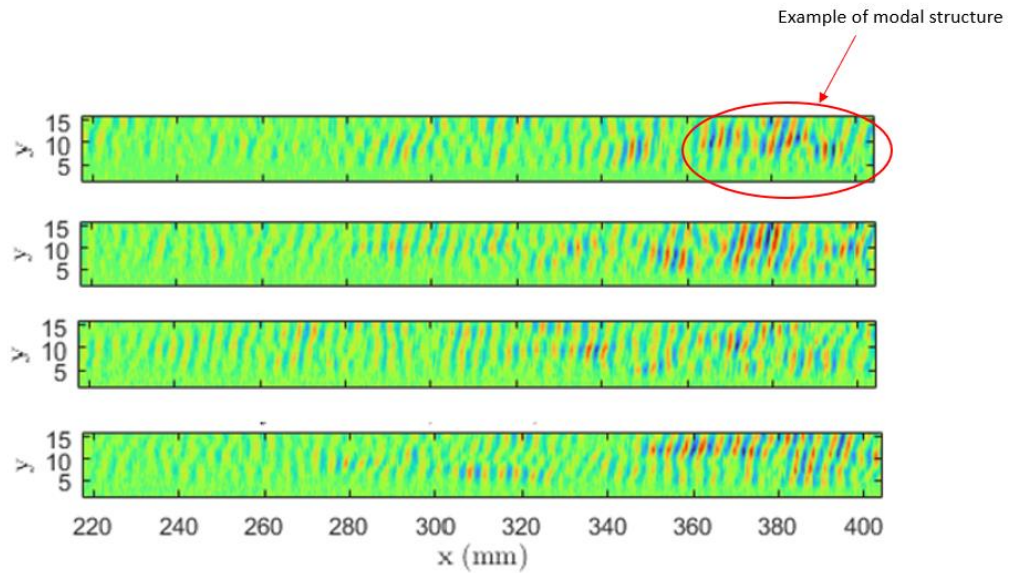
Figure 34. SPOD spectra images captured at various frequencies (from the top, 200 kHz, 206 kHz, 214 kHz and 225 kHz)

Chapter 5

Conclusion and Further Work

5.1   Conclusion

A seven-degree half angle model has been manufactured and mounted at a zero angle of attack in TUSQ for analysis. Two runs have been observed with separate configurations such as run 1229 consisting of four sensors in positions D, E, F, G and run 1372 with a full suite of seven sensors installed. Run 1229 included the application of the high-speed camera, Phantom TMX-7510 on loan from Adept Turnkey. The schlieren images were captured at 450,000 fps.

High speed pressure fluctuations measured at discrete locations along one azimuthal ray of the model surface shows the second mode growth along the cone as an increase of energy within the 200-300 kHz band. The peak energy decreased with distance along the cone surface showing consistency with second mode instability propagating a boundary layer of increasing thickness.

SPOD was utilised as the method of analysis to investigate the most energetic modal frequency and modal structures. SPOD eigenvalues for each mode as a function of frequency have been obtained and graphed as a SPOD energy spectra. The SPOD energy spectra plot shown in Figure 34 asserts that dominant structures have not been identified in the SPOD analysis. In comparison of the PCB data, an increase in modal energy from 200 kHz is expected however, not apparent in this analysis. Windowing of the schlieren images to the vicinity of the PCBs was conducted as an alternative method for the SPOD analysis however, the SPOD energy spectrum exhibited no clear increase due to the second mode instability. Schlieren imaging was recorded at 450,000 fps therefore, the maximum frequency that could be resolved was 225 kHz. This is insufficiently high to resolve the entire energy spectrum containing the second mode. However, the SPOD produced power spectral density plots should have resolved the portion of the second-mode instability below 225 kHz.

SPOD spectra images were obtained, and modal structure was successfully studied. Clear rope like structure is observed suggesting that second mode instabilities within the boundary layer exist. The greatest challenge for further development of a schlieren imaging based method for study of the second mode instability in TUSQ is hardware.

A high speed camera with an ideal frame rate of at least 560,000 fps and laser source capability could be explored to determine how many pulses at 560,000 Hz and 10 ns duration can be produced within the laser controller functionality. This investigation requires the procurement of high performance photodetectors for the completion of this work. However, SPOD spectra images suggest that there is scope to revisit this analysis.

It is noted that this experiment was a one-off facility run. Although the inbuild frequency analysis did not produce useful results, SPOD may be useful for future modal structure studies.

5.2   Further Work

Further work on Spectral Proper Orthogonal Decomposition analysis in the TUSQ facility may follow from this study in the areas identified with the most feasible for short term results including further experience development with the SPOD method. I recommend application of the method to the study of features and structure of frequencies between 500 Hz and 15 kHz. The lower bound will enable sufficient cycles within the full duration, while the upper frequency bound is within the continuous operation limits of the current hardware.

Suitable studies could be vortex shredding, recirculation behind the rearward facing step or, fluid structure interactions. The fluid structure interaction study may require decoupling of the structure motion from the SPOD analysis.

Bibliography

Anderson, JJ 1984, 'A survey of modern research in hypersonic aerodynamics', in *17th Fluid Dynamics, Plasma Dynamics, and Lasers Conference*, American Institute of Aeronautics and Astronautics.

Birch, B 2019, 'Characterisation of the USQ Hypersonic Facility Freestream', PhD thesis, University of Southern Queensland, Toowoomba, Queensland.

Birch, B, Buttsworth, D, Choudhury, R & Stern, N 2018, 'Characterization of a Ludwieg Tube with Free Piston Compression Heating in Mach 6 Configuration', in *22nd AIAA International Space Planes and Hypersonics Systems and Technologies Conference*, American Institute of Aeronautics and Astronautics.

Buttsworth, D 2009, 'Ludwieg tunnel facility with free piston compression heating for supersonic and hypersonic testing', *Australian space science conference*, National Space Society of Australia Ltd, Sydney, pp. 153-62.

Buttsworth, D & Smart, M 2010, 'Development of a Ludwieg Tube with Free Piston Compression Heating for Scramjet Inlet Starting Experiments', in *48th AIAA Aerospace Sciences Meeting Including the New Horizons Forum and Aerospace Exposition*, American Institute of Aeronautics and Astronautics.

Cammilleri, A, Gueniat, F, Carlier, J, Pastur, L, Memin, E, Lusseyran, F & Artana, G 2013, 'POD-spectral decomposition for fluid flow analysis and model reduction', *Theoretical and computational fluid dynamics*, vol. 27, no. 6, pp. 787-815.

Cengel, YA, Cimbala, J & Turner, RH 2017, *Fundamentals of Thermofluid Sciences in SI Units*, 5th edn, McGraw Education, New York.

Clemens, NT & Narayanaswamy, V 2014, 'Low-Frequency Unsteadiness of Shock Wave Turbulent Boundary Layer Interactions', *Annual review of fluid mechanics*, vol. 46, no. 1, pp. 469-92.

Combs, CS, Lash, EL & Schmisseur, JD 2016, 'Investigation of a Cylinder-Induced Transitional Shock Wave-Boundary Layer Interaction using Laser Diagnostics', in *32nd AIAA Aerodynamic Measurement Technology and Ground Testing Conference*, American Institute of Aeronautics and Astronautics.

Combs, CS, Kreth, PA, Schmisseur, JD & Lash, EL 2017, 'Image-Based Analysis of Shock-Wave/Boundary-Layer Interaction Unsteadiness', *AIAA Journal*, vol. 56, no. 3, pp. 1288-93.

Cottier, SM 2019, 'Spectral Proper Orthogonal Decomposition Analysis of Shock-wave/Boundary-layer Interactions', ProQuest Dissertations Publishing.

Estruch, D, MacManus, DG, Richardson, DP, Lawson, NJ, Garry, KP & Stollery, JL 2010, 'Experimental study of unsteadiness in supersonic shock-wave/turbulent boundary-layer interactions with separation', *Aeronautical journal*, vol. 114, no. 1155, pp. 299-308.

Fedorov, A 2011, 'Transition and stability of high-speed boundary layers', *Annual review of fluid mechanics*, vol. 43, no. 1, pp. 79-95.

Floryan, JM 1991, 'On the görtler instability of boundary layers', *Progress in aerospace sciences*, vol. 28, no. 3, pp. 235-71.

Gaitonde, DV 2015, 'Progress in shock wave/boundary layer interactions', *Progress in aerospace sciences*, vol. 72, pp. 80-99.

Hyslop, AM, McGilvray, M & Doherty, LJ 2021, 'Free-Flight Aerodynamic Testing of a 7 Degree Half-Angle Cone', in *AIAA SCITECH 2022 Forum*, American Institute of Aeronautics and Astronautics.

Iyer, PS 2015, 'Discrete Roughness Effects on High-Speed Boundary Layers', ProQuest Dissertations Publishing.

Jones, T, Schultz, D & Hendley, A 1973, 'On the flow in an Isentropic Light Piston Tunnel', *Aeronautical Research Council, Reports and Memoranda*.

Knisely, CP & Zhong, X 2019, 'Significant Supersonic Modes and the Wall Temperature Effect in Hypersonic Boundary Layers', *AIAA Journal*, vol. 57, no. 4, pp. 1552-66.

Kuehl, JJ 2018, 'Thermoacoustic Interpretation of Second-Mode Instability', *AIAA Journal*, vol. 56, no. 9, pp. 3585-92.

Kunihiko, T, Steven, LB, Scott, TMD, Clarence, WR, Tim, C, Beverley, JM, Oliver, TS, Stanislav, G, Vassilios, T & Lawrence, SU 2017, *Modal Analysis of Fluid Flows: An Overview*, Cornell University Library, arXiv.org, Ithaca, 2331-8422.

Laurence, SJ, Wagner, A & Hannemann, K 2016, 'Experimental study of second-mode instability growth and breakdown in a hypersonic boundary layer using high-speed schlieren visualization', *Journal of fluid mechanics*, vol. 797, pp. 471-503.

Loginov, MS, Adams, NA & Zheltovodov, AA 2006, 'Large-eddy simulation of shock-wave/turbulent-boundary-layer interaction', *Journal of fluid mechanics*, vol. 565, pp. 135-69.

Lumley, JL 1967, 'The Structure of Inhomogeneous Turbulent Flows', *Atmospheric Turbulence and Radio Wave Propagation*.

Mack, LM 1975, 'Linear Stability Theory and the Problem of Supersonic Boundary- Layer Transition', *AIAA Journal*, vol. 13, no. 3, pp. 278-89.

Marineau, EC, Grossir, G, Wagner, A, Leinemann, M, Radespiel, R, Tanno, H, Wadhams, TP, Chynoweth, BC, Schneider, SP, Wagnild, R & Casper, KM 2018, 'Compilation and Analysis of Second Mode Amplitudes on Sharp Cones in Hypersonic Wind Tunnels', in *2018 AIAA Aerospace Sciences Meeting*, American Institute of Aeronautics and Astronautics.

Martin, P, Priebe, S & Wu, M 2008, 'Upstream and downstream influence on the unsteadiness of STBLI using DNS data in two configurations', in *46th AIAA Aerospace Sciences Meeting and Exhibit*, American Institute of Aeronautics and Astronautics.

Murphree, Z, Jagodzinski, J, Hood, E, Clemens, N & Dolling, D 2006, 'Experimental Studies of Transitional Boundary Layer Shock Wave Interactions', in *44th AIAA Aerospace Sciences Meeting and Exhibit*, American Institute of Aeronautics and Astronautics.

Nichols, JW, Larsson, J, Bernardini, M & Pirozzoli, S 2016, 'Stability and modal analysis of shock/boundary layer interactions', *Theoretical and computational fluid dynamics*, vol. 31, no. 1, pp. 33-50.

Picard, C & Delville, J 2000, 'Pressure velocity coupling in a subsonic round jet', *The International journal of heat and fluid flow*, vol. 21, no. 3, pp. 359-64.

Priebe, S, Tu, JH, Rowley, CW & Martín, MP 2016, 'Low-frequency dynamics in a shock-induced separated flow', *Journal of fluid mechanics*, vol. 807, pp. 441-77.

Pritchard, PJ 2011, *Fox and Mcdonalds Introduction to Fluid Mechanics*, 8th edn, John Wiley & Sons, United States of America.

Ramasamy, M, Sanayei, A, Wilson, J, Martin, P, Harms, T, Nikoueeyan, P & Naughton, J 2019, *Data-Driven Optimal Basis Clustering To Characterize Cycle-to-Cycle Variations in Dynamic Stall Measurements*.

Schmid, PJ 2010, 'Dynamic mode decomposition of numerical and experimental data', *Journal of fluid mechanics*, vol. 656, no. August, pp. 5-28.

Schmidt, OT & Towne, A 2019, 'An efficient streaming algorithm for spectral proper orthogonal decomposition', *Computer physics communications*, vol. 237, pp. 98-109.

Sirovich, L 1987, 'Turbulence and the dynamics of coherent structures. I - Coherent structures. II - Symmetries and transformations. III - Dynamics and scaling', *Quarterly of Applied Mathematics - QUART APPL MATH*, vol. 45.

Tinney, CE & Jordan, P 2008, 'The near pressure field of co-axial subsonic jets', *Journal of fluid mechanics*, vol. 611, pp. 175-204.

Towne, A, Schmidt, OT & Colonius, T 2018, 'Spectral proper orthogonal decomposition and its relationship to dynamic mode decomposition and resolvent analysis', *Journal of fluid mechanics*, vol. 847, pp. 821-67.

Tutkun, M & George, WK 2017, 'Lumley decomposition of turbulent boundary layer at high Reynolds numbers', *Physics of Fluids*, vol. 29, no. 2, p. 020707.

Vanstone, L & Clemens, NT 2019a, 'Unsteadiness Mechanisms of a Swept Compression-Ramp Shock / Boundary Layer Interaction at Mach 2', in *AIAA Scitech 2019 Forum*, American Institute of Aeronautics and Astronautics.

Vanstone, L & Clemens, NT 2019b, 'Proper Orthogonal Decomposition Analysis of Swept-Ramp Shock-Wave/Boundary-Layer Unsteadiness at Mach 2', *AIAA Journal*, vol. 57, no. 8, pp. 3395-409.

Webb, A, Birch, B, Zander, F & Buttsworth, D 2022, 'Transitional Boundary Layer Measurements in the University of Southern Queensland Hypersonic Wind Tunnel', *23rd Australasian Fluid Mechanics Conference (AFMC2022)*: *Proceedings of the 23rd Australasian Fluid Mechanics Conference (AFMC2022)* University of Sydney, Sydney, Australia.

Weiss, J 2019, 'A Tutorial on the Proper Orthogonal Decomposition', in *AIAA Aviation 2019 Forum*, American Institute of Aeronautics and Astronautics.

Zhong, X & Wang, X 2012, 'Direct Numerical Simulation on the Receptivity, Instability, and Transition of Hypersonic Boundary Layers', *Annual review of fluid mechanics*, vol. 44, no. 1, pp. 527-61.

Appendix

Appendix A - Project Specification

ENG 4111/4112 Research Project

Project Specification

For: Adam Smith

Title: Spectral Proper Orthogonal Decomposition of High Speed Schlieren Images

Major: Mechanical

Supervisors: Dr. Byrenn Birch

Enrollment: ENG4111 – EXT S1, 2023

              ENG4112 – EXT S2, 2023

Project Aim: The project aim is to use spectral proper orthogonal decomposition (SPOD) for the investigation of the flow around models which are mounted in the University of Southern Queensland's Hypersonic Wind tunnel (TUSQ). The primary objective is to apply the SPOD technique to the study of second-mode instabilities, imaged using high-speed schlieren, in the boundary layer of a slender cone at Mach 6. The analysis should reveal the most energetic modal frequency and structures. The SPOD results will be compared to high-speed surface pressure fluctuations which are measured at discrete locations along the one azimuthal ray of the model surface.

Programme: Version 2, 20th February 2023

1. Research the necessary background information on hypersonic flow theory and schlieren image analysis.

2. Review the Spectral Proper Orthogonal Decomposition (SPOD) method and understand the numerical inputs.

3. Install MATLAB utilising the UniSQ campus licence and review the SPOD examples to understand the method.

4. Communicate with relevant hypersonic staff with respect to historical experimental data from the TUSQ facility for a 7-degree half-angle cone.

5. Perform the SPOD technique and identify where the local frequency content will be quantified with respect to the boundary layer interactions.
6. Compare the SPOD results to high-frequency surface pressure measurements.

If time and resource permit:

7. Apply the SPOD technique to schlieren imaging using a particle image velocimetry (PIV) like pulse train.
8. Use SPOD to investigate the freestream density fluctuations in TUSQ. A 3-4 kHz narrowband fluctuation is known to appear after about 65 ms of flow.

Appendix B - Project Requirements

ENG 4111/4112 Research Project

Project Resources

Requirements:

- Access to an adequate computer to be used for research with respect to the literature review, processing the dissertation document and analysing results – This is already in the students possession.
- The student is required to access the UniSQ campus wide MATLAB licence and install on their machine furthermore, refresh their knowledge on the program.
- Planning with respect to organising the appropriate required experimental data to complete the project. This involves effective communication with TUSQ engineering staff – This data has now been collected.
- Experimental testing within the TUSQ hypersonic wind tunnel where, prior organisation will be required with the students supervisor and TUSQ engineering staff. This will likely be a piggy-back arrangement from a current PhD students work.

Appendix C - Project Plan

ID	Task Name	Duration	Start	Finish	Predecessors
1	**Final reseach dissertation**	192 days	Thu 26/01/23	Fri 20/10/23	
2	Project Proposal form	6 days	Thu 26/01/23	Thu 2/02/23	
3	Project Specification	16 days	Fri 3/02/23	Fri 24/02/23	2
4	Feedback for Project Specification	6 days	Fri 24/02/23	Fri 3/03/23	2
5	Progress Report	63 days	Mon 27/02/23	Wed 24/05/23	3
6	Complete SPOD tutorials	13 days	Mon 27/02/23	Wed 15/03/23	
7	Produce preliminary results for review	26 days	Thu 16/03/23	Thu 20/04/23	6
8	Progress Report feedback	11 days	Thu 25/05/23	Thu 8/06/23	5
9	Produce plots for the run of interest for review by supervisor	12 days	Thu 27/07/23	Fri 11/08/23	
10	Draft submission	68 days	Fri 9/06/23	Tue 12/09/23	8
11	Professional Practice 2	5 days	Mon 18/09/23	Fri 22/09/23	
12	Final review of dissertation	28 days	Wed 13/09/23	Fri 20/10/23	8,10

Appendix D - Risk Assessment

Note: This is the offline version of the Safety Risk Management System (SRMS) Risk Management Plan (RMP) and is only to be used for planning and drafting sessions, and when working in remote areas or on field activities. It must be transferred to the online SRMS at the first opportunity.

Safety Risk Management Plan – Offline Version				
Assessment Title:	ENG4111/ENG4112 Dissertation		Assessment Date:	1/10/2022
Workplace (Division/Faculty/Section):	Faculty of Health, Engineering and Sciences		Review Date:(5 Years Max)	1/10/2027
Context				
Description:				
What is the task/event/purchase/project/procedure?		Task associated with final project for BEng(Hons)		
Why is it being conducted?	Assessment procedure for the successful completion for the program BEng(Hons)			
Where is it being conducted?	Waterford/Toowoomba, Qld			
Course code (if applicable)	ENG4111/ENG4112		Chemical name (if applicable)	Air
What other nominal conditions?				
Personnel involved	Adam Smith			

Equipment	Computer, General hand tools, TUSQ wind tunnel
Environment	My home, P10, protected from elements - dry
Other	NA
Briefly explain the procedure/process	Mostly research and study based on a computer. If time permits, project will involve testing in P10. All relevant procedures for the lab to be followed.
Assessment Team - who is conducting the assessment?	
Assessor(s)	Adam Smith
Others consulted	NA

Eg 1. Enter Consequence

Probability	Consequence				
	Insignificant No Injury 0-$5K	**Minor** First Aid $5K-$50K	**Moderate** Med Treatment $50K-$100K	**Major** Serious Injuries $100K-$250K	**Catastrophic** Death More than $250K
Almost Certain 1 in 2	M	H	E	E	E
Likely 1 in 100	M	H	H	E	E
Possible 1 in 1000	L	M	H	H	H
Unlikely 1 in 10 000	L	L	M	M	M
Rare 1 in 1 000 000	L	L	L	L	L

Eg 2. Enter Probability

Recommended Action Guide

E=Extreme Risk – Task *MUST NOT* proceed

H=High Risk – Special Procedures Required (See USQSafe)

M=Moderate Risk – Risk Management Plan/Work Method Statement Required

L=Low Risk – Use Routine Procedures

Eg 3. Find Action

Step 1 (cont)	Step 2	Step 2a	Step 2b	Step 3			Step 4				
Hazards: From step 1 or more if identified	*The Risk:* What can happen if exposed to the hazard without existing controls in place?	*Consequence:* What is the harm that can be caused by the hazard without existing controls in place?	*Existing Controls:* What are the existing controls that are already in place?	*Risk Assessment:* Consequence x Probability = Risk Level			*Additional controls:* Enter additional controls if required to reduce the risk level	*Risk assessment with additional controls:*			
				Probability	Risk Level	ALARP? Yes/no		Consequence	Probability	Risk Level	ALARP? Yes/no
Example											
Working in temperatures over 35⁰ C	Heat stress/heat stroke/exhaustion leading to serious personal injury/death	catastrophic	Regular breaks, chilled water available, loose clothing, fatigue management policy.	possible	high	No	temporary shade shelters, essential tasks only, close supervision, buddy system	catastrophic	unlikely	mod	Yes
Excessive time spent at computer	Eyestrain/muscle tension or pain/risk of blood clotting	Minor	Ensure adequate breaks are included in study sessions	Unlikely	Low	Yes or No		Select a consequence	Select a probability	Select a Risk Level	Yes or No
Trip hazards in lab	Head injury/broken bones/cuts all leading to serious injury	Minor	Maintain good housekeeping Do not block walkways Ensure cables are correctly stored	Unlikely	Low	Yes or No		Select a consequence	Select a probability	Select a Risk Level	Yes or No
Pressurised air	Eye injury/injury or death to personal if held against skin	Minor	Never point air fittings towards operators Timed release of air when undertaking testing The operator should not leave workspace until air is fully discharged	Unlikely	Low	Yes or No		Select a consequence	Select a probability	Select a Risk Level	Yes or No
Sharp edges on hypersonic model	Cuts or lacerations to personal/potential to catch and cut clothing	Minor	Allows store the model with a rubber protector over the sharp corner and only remove for testing Once assembled for	Unlikely	Low	Yes or No		Select a consequence	Select a probability	Select a Risk Level	Yes or No

Step 1 (cont)	Step 2	Step 2a	Step 2b	Step 3			Step 4				
Hazards: From step 1 or more if identified	*The Risk:* What can happen if exposed to the hazard without existing controls in place?	*Consequence:* What is the harm that can be caused by the hazard without existing controls in place?	*Existing Controls:* What are the existing controls that are already in place?	*Risk Assessment:* Consequence x Probability = Risk Level			*Additional controls:* Enter additional controls if required to reduce the risk level	*Risk assessment with additional controls:*			
				Probability	**Risk Level**	**ALARP? Yes/no**		**Consequence**	**Probability**	**Risk Level**	**ALARP? Yes/no**
Example											
Working in temperatures over 35⁰ C	Heat stress/heat stroke/exhaustion leading to serious personal injury/death	catastrophic	Regular breaks, chilled water available, loose clothing, fatigue management policy.	possible	high	No	temporary shade shelters, essential tasks only, close supervision, buddy system	catastrophic	unlikely	mod	Yes
			testing, the test section is not assessable								
		Select a consequence		Select a probability	Select a Risk Level	Yes or No		Select a consequence	Select a probability	Select a Risk Level	Yes or No
		Select a consequence		Select a probability	Select a Risk Level	Yes or No		Select a consequence	Select a probability	Select a Risk Level	Yes or No
		Select a consequence		Select a probability	Select a Risk Level	Yes or No		Select a consequence	Select a probability	Select a Risk Level	Yes or No
		Select a consequence		Select a probability	Select a Risk Level	Yes or No		Select a consequence	Select a probability	Select a Risk Level	Yes or No
		Select a consequence		Select a probability	Select a Risk Level	Yes or No		Select a consequence	Select a probability	Select a Risk Level	Yes or No
		Select a consequence		Select a probability	Select a Risk Level	Yes or No		Select a consequence	Select a probability	Select a Risk Level	Yes or No
		Select a consequence		Select a probability	Select a Risk Level	Yes or No		Select a consequence	Select a probability	Select a Risk Level	Yes or No
		Select a consequence		Select a probability	Select a Risk Level	Yes or No		Select a consequence	Select a probability	Select a Risk Level	Yes or No
		Select a consequence		Select a probability	Select a Risk Level	Yes or No		Select a consequence	Select a probability	Select a Risk Level	Yes or No
				Select a probability	Select a Risk Level	Yes or No		Select a consequence	Select a probability	Select a Risk Level	Yes or No
				Select a probability	Select a Risk Level	Yes or No		Select a consequence	Select a probability	Select a Risk Level	Yes or No
				Select a probability	Select a Risk Level	Yes or No		Select a consequence	Select a probability	Select a Risk Level	Yes or No

Step 5 - Action Plan (for controls not already in place)			
Additional controls:	*Resources:*	*Persons responsible:*	*Proposed implementation date:*
			Click here to enter a date.
			Click here to enter a date.
			Click here to enter a date.
			Click here to enter a date.
			Click here to enter a date.
			Click here to enter a date.
			Click here to enter a date.
			Click here to enter a date.
			Click here to enter a date.
			Click here to enter a date.
			Click here to enter a date.
			Click here to enter a date.

Step 6 - Approval

Drafter's name:	Adam Smith	Draft date:	1/10/2022
Drafter's comments:	NA		
Approver's name:		Approver's title/position:	
Approver's comments:			
I am satisfied that the risks are as low as reasonably practicable and that the resources required will be provided.			
Approver's signature:		Approval date:	Click here to enter a date.

Appendix E – Manufacturing Drawing Modifications

MATERIAL: 630 STAINLESS STEEL
NUMBER REQ: 1

M8 TO DEPTH AS SHOWN

SHARP

R0.4

1 x 45°

0.5 x 45°

$\varnothing$12.50 $^{+0.03}_{+0.01}$ $\varnothing$18.42 $^{+0.02}_{-0.00}$

0.00

7.6

21.6

7.0°

75.00 INT

HAND FINISH R0.2
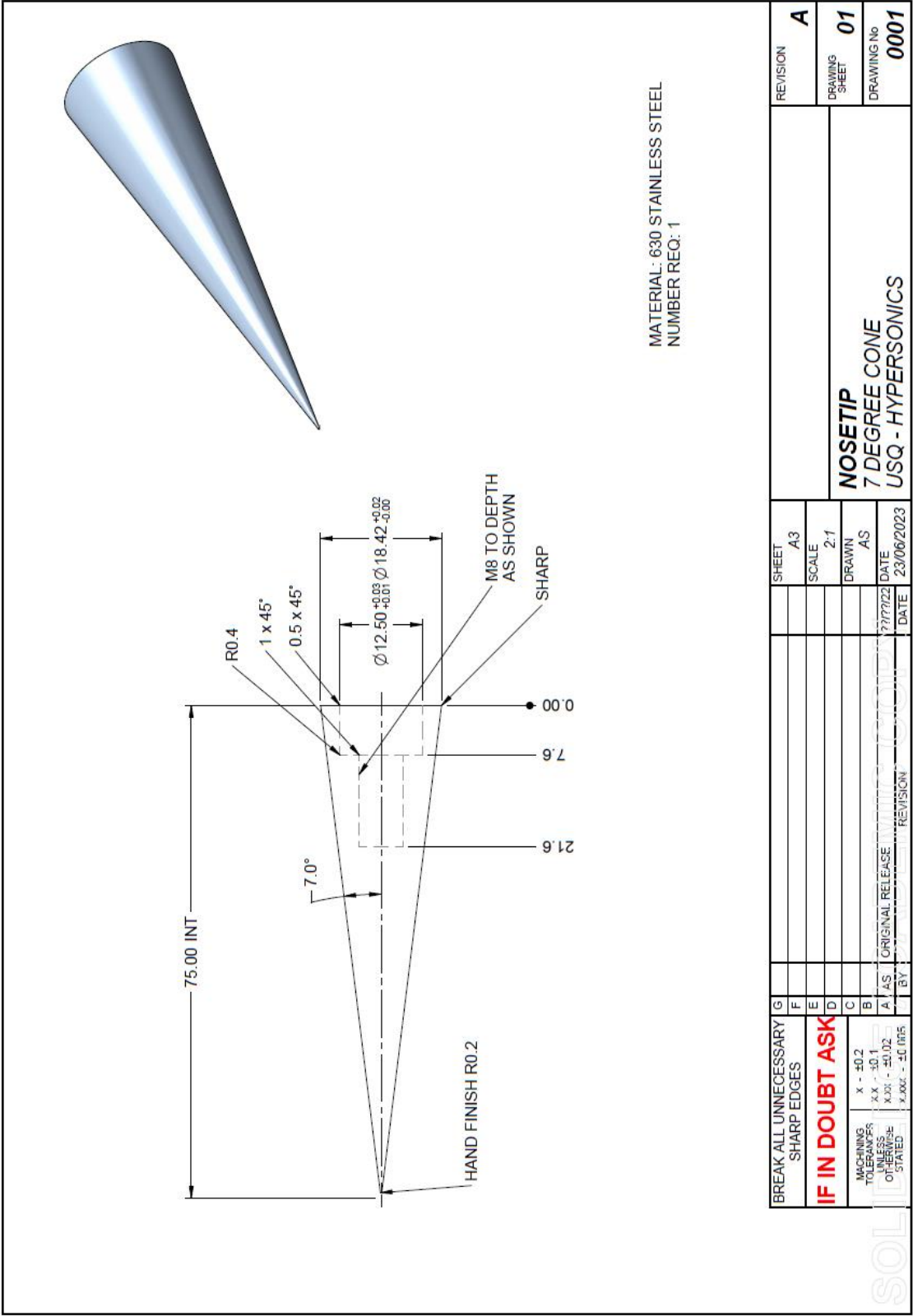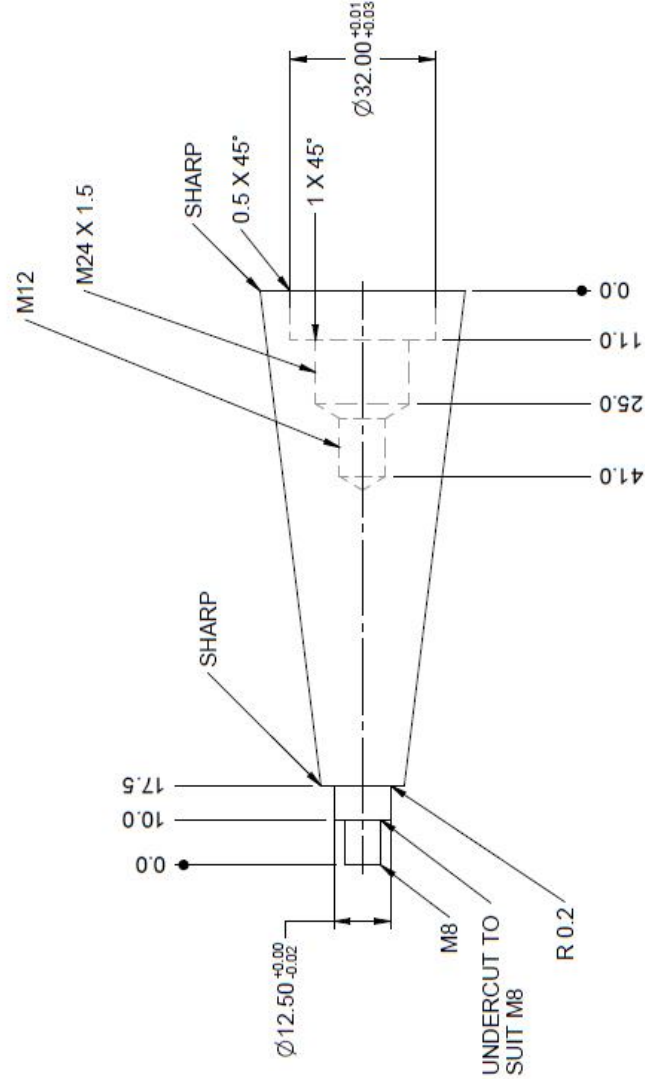
BREAK ALL UNNECESSARY SHARP EDGES	G		SHEET	A3		REVISION	*A*
	F						
	E		SCALE	2:1		DRAWING SHEET	*01*
IF IN DOUBT ASK	D		DRAWN	AS		DRAWING No	*0001*
MACHINING TOLERANCES		X.X = ±0.2	C				
UNLESS OTHERWISE STATED	X.X = ±0.1	B					
	X.XX = ±0.02	A	AS	ORIGINAL RELEASE	DATE 23/06/2023		
	X.XXX = ±0.005		BY	REVISION	DATE ??/??/22		

NOSETIP
7 DEGREE CONE
USQ - HYPERSONICS

MATERIAL: 630 STAINLESS STEEL
NUMBER REQ: 1

Ø32.00 +0.01 +0.03

SHARP
0.5 X 45°
1 X 45°

M24 X 1.5
M12

0.0
11.0
25.0
41.0

SHARP

17.5
10.0
0.0

Ø12.50 +0.00 -0.02

M8
UNDERCUT TO SUIT M8
R 0.2

BREAK ALL UNNECESSARY SHARP EDGES

IF IN DOUBT ASK

MACHINING TOLERANCES UNLESS OTHERWISE STATED	x - ±0.2
	x.x - ±0.1
	x.xx - ±0.02
	x.xxx - ±0.005

G					
F					
E					
D					
C					
B					
A	AS	ORIGINAL RELEASE			
	BY	REVISION			

?/??/22 ORIGINAL RELEASE

SHEET	A3
SCALE	1:1
DRAWN	AS	DATE	?/??/22
		DATE	9/07/2023

SPACER
7 DEGREE CONE
USQ - HYPERSONICS

REVISION   A

DRAWING SHEET   01

DRAWING No   0002

19.50 $^{+0.02}_{-0.00}$ TYP

$\varnothing$9.50 $^{+0.02}_{-0.00}$ TYP

9.50 $^{+0.02}_{-0.00}$ TYP

M3
14 PLACES

$\varnothing$6.50 $^{+0.02}_{-0.00}$
8 PLACES

R0.2

M24 X 1.5

1.5 X 45°

UNDERCUT TO
SUIT M24 X 1.5

SHARP

$\varnothing$32.00 $^{+0.00}_{-0.05}$

MATERIAL: 630 STAINLESS STEEL
NUMBER REQ: 1

BREAK ALL UNNECESSARY	G		
SHARP EDGES	F		
	E		
IF IN DOUBT ASK	D		
	C		
	B		
MACHINING TOLERANCES:	A	AS	ORIGINAL RELEASE.
UNLESS OTHERWISE STATED		BY	REVISION

MACHINING TOLERANCES:	
x - ±0.2	
x.x - ±0.1	
x.xx - ±0.02	
x.xxx - ±0.005	

SHEET	A3
SCALE	1:1
DRAWN	AS
DATE	15/07/23
DATE	15/07/2023

UPPER REAR FRUSTRUM
7 DEGREE CONE
USQ - HYPERSONICS

REVISION **A**

DRAWING SHEET **01**

DRAWING No **1003**

MACHINE INTERNAL
FORM AS PER 1003
UPPER REAR FRUSTRUM

Ø6.50 $^{+0.00}_{-0.01}$
8 PLACES

CLEARANCE FOR
M12 SHCS ONLY

SHARP

R0.2

Ø13.0 DRILL

Ø32.00 $^{+0.00}_{-0.05}$

MATERIAL: BLACK ACETAL
NUMBER REQ: 1

BREAK ALL UNNECESSARY
SHARP EDGES

IF IN DOUBT ASK

MACHINING TOLERANCES UNLESS OTHERWISE STATED	x - ±0.2
	x.x - ±0.1
	x.xx - ±0.02
	x.xxx - ±0.005

G			
F			
E			
D			
C			
B			
A	AS	ORIGINAL RELEASE	17/07/23
	BY	REVISION	DATE

SHEET	A3
SCALE	1:1
DRAWN	AS
DATE	17/07/2023

ASSEMBLY LAYOUT
7 DEGREE CONE
USQ - HYPERSONICS

REVISION	A
DRAWING SHEET	01
DRAWING No	0003

R0.2
3 PLACES

UNDERCUT TO
SUIT M18

1.5 X 45°

Ø20.0 +0.00 -0.10

Ø6.5 DRILL

M18

0.5 X 45°

Ø8.2 DRILL

CAN BE DRILL ANGLE

SECTION A-A

Ø8.4 DRILL
12 PLACES

A

A

Ø85.0

MATERIAL: 4140 - FLASH CHROME
NUMBER REQ: 1

MACHINE Ø3.3 HOLE
WHEN ASSEMBLED
IN FINAL PROCESS

Ø9.50 -0.01 -0.02

0.00

MACHINE BLANK
FINSH TURN WHEN
ASSEMBLED IN
UPPER REAR FRUSTRUM

R.4

9.75

0.3

6.56

Ø5.0

Ø3.2 DRILL
2 PLACES

9.50 -0.01 -0.02

19.50 -0.01 -0.02

MATERIAL: 630 STAINLESS STEEL
NUMBER REQ: 7 - LASER ENGRAVE "A" - "G"

BREAK ALL UNNECESSARY SHARP EDGES	G			SHEET	A3		INSERT
	F						7 DEGREE CONE
IF IN DOUBT ASK	E			SCALE	5:1		USQ - HYPERSONICS
	D						
MACHINING TOLERANCE UNLESS OTHERWISE STATED	C			DRAWN	AS		
x - ±0.2	B			DATE	18/07/2023		
x.x - ±0.1	A	AS	18/07/23	ORIGINAL RELEASE		REVISION	A
x.xx - ±0.02		BY	DATE	REVISION		DRAWING SHEET	01
x.xxx - ±0.005						DRAWING No	8000

Appendix F – Manufacturing Process Photos

Figure I 1. Rough turned Nosetips prior to finish grinding including manufactured Nosetip fixture.
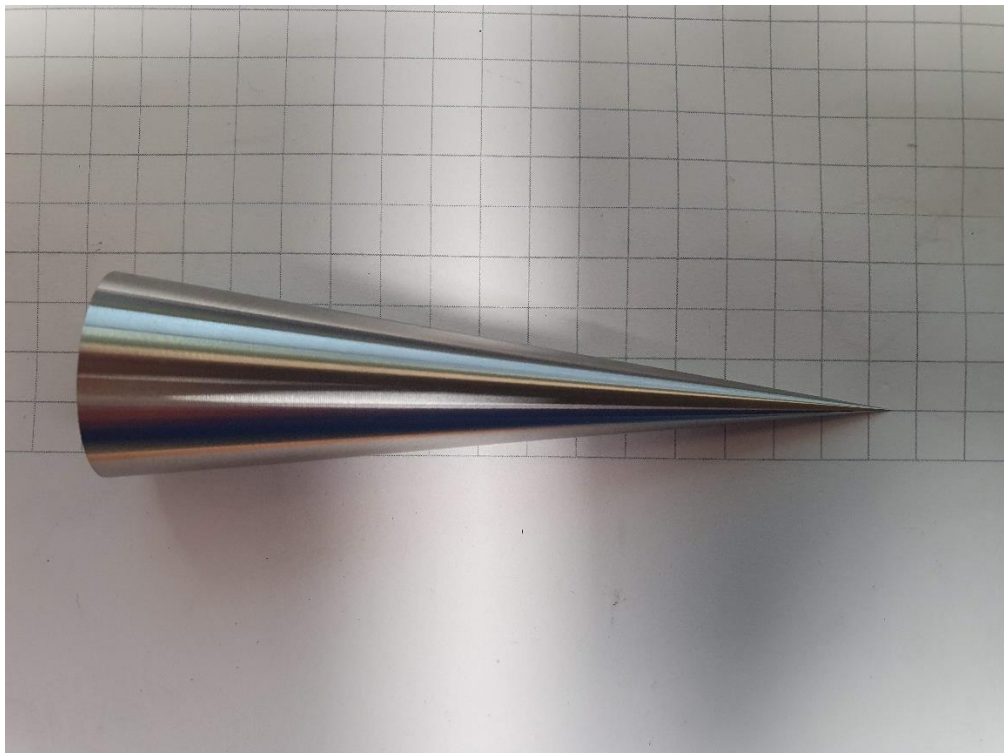

Figure I 2. Finish ground Nosetip

Figure I 3. Example of completed R0.05 Nosetip - Scale 20:1

Figure F 4. Manufacturing process photo including intermediate frustrum, sting mount, upper rear frustrum inserts and fixture components.

Figure F 5. In process photo of the upper rear frustrum prior to machining in half.

Figure F 6. Upper rear frustrum with assembled inserts and dowel pins (left) Lower rear frustrum machined from Acetal (right)

Figure F 7. Assembled rear frustrums and intermediate frustrum fitted with turning centre for 7 degree finish turning

Figure F 8. Assembled 7 degree half cone - lower rear frustrum focus

Figure F 9. Assembled 7 degree half cone - upper rear frustrum focus

Appendix G – TUSQ barrel pressure for run 1229

A barrel pressure trace that has been configured to the point in time where the diaphragm ruptures, t = 0 for the run of interest is show in Figure G 1. The trace shows the gradual opening of the valve from ~1000 ms. The test gas is compressed as the piston accelerates within the tube with the rupture of a diaphragm shown at approximately 0.95 MPa.
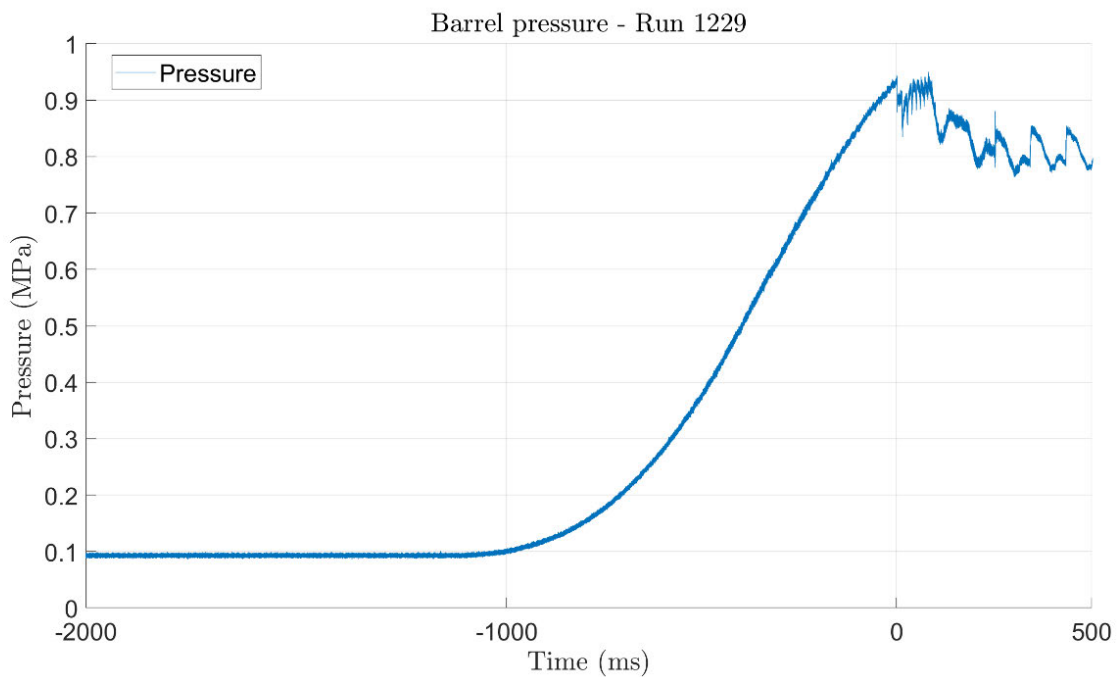

Figure G 1. Barrel pressure for complete run 1229